Following the photons route: mathematical models describing the interaction of diatoms with light

Edoardo De Tommasi,[1] Alessandra Rogato,[2,3] Diego Caratelli,[4,5] Luciano Mescia,[6] and Johan Gielis[5,7]

[1]Institute of Applied Sciences and Intelligent Systems, National Research Council, Naples, Italy

[2]Institute of Biosciences and Bioresources, National Research Council, Naples, Italy

[3]Department of Integrative Marine Ecology, Stazione Zoologica Anton Dohrn, Naples, Italy

[4]Department of Research and Development, The Antenna Company, High Tech Campus 29, 5656 AE Eindhoven, The Netherlands

[5]Department of Electrical Engineering, Eindhoven University of Technology, PO Box 513, 5600 MB Eindhoven, The Netherlands

[6] Polytechnic University of Bari, Via E. Orabona, 4, 70125 Bari, Italy

[7]Dept of Bioscience Engineering, University of Antwerp, Groenenborgerlaan 171, 2020 Antwerp, Belgium

Abstract

The interaction of diatoms with sunlight is fundamental in order to deeply understand their role in terrestrial ecology and biogeochemistry, essentially due to their massive contribution to global primary production through photosynthesis and its effect on carbon, oxygen and silicon cycles. Following the journey of light through natural waters, its propagation through the intricate frustule micro- and nano-structure and, finally, its fate inside the photosynthetic machinery of the living cell requires several mathematical and computational models in order to accurately describe all the involved phenomena taking place at different space scales and physical regimes.

In this chapter, we review the main analytical models describing the underwater optical field, the essential numerical algorithms for the study of photonic properties of the diatom frustule seen as a natural metamaterial, as well as the principal models describing photon harvesting in diatom plastids and methods for complex EM propagation problems and wave propagation in dispersive materials with multiple relaxation times. These mathematical methods will be integrated in a unifying geometric perspective.

1 Introduction

Almost all aquatic habitats on Earth are colonized by diatoms [Seckbach and Kociolek, 2011]. Being the most common type of phytoplankton, they contribute massively to global primary production (up to 20-25%) [Leblanc et al., 2018], fixing large amounts of carbon dioxide in the oceans, in freshwater, and generally wherever water is at least occasionally present. Understanding the mechanisms by which diatoms interact with sunlight is the key to unveil the origin of their extraordinary photosynthetic efficiency and evolutionary success. The exchanges between diatoms and external environment are mediated by the frustule, a porous, hydrated silica investment which encloses the cell and is characterized by the presence of regular patterns of pores. Frustules are at the basis of diatom taxonomy [Round et al., 1990], and their huge variety of shapes and dimensions (ranging from some tens of microns to 1-2 millimeters) allows distinguishing up to more than 10^3 genera and about 10^5 species [Smol and Stoermer, 2010]. They basically consist in an *epitheca* overlapping a *hypotheca* in a "petri-dish-like" arrangement. Every *theca* is formed by a valve and one or more lateral bands (girdle bands) connected along the margins. Frustule functionalities comprise mechanical protection [Hamm et al., 2003], gas exchange [Emerson and Hedges, 2008], sorting of nutrients from noxious agents such as viruses [Hale and Mitchell, 2001], and sinking rate control [Waite et al., 1997]. The impressive similarity of diatom frustules with artificial photonic crystals induced to deepen also their optical properties, including the ability to couple light in waveguided modes [Fuhrmann et al., 2004], to collect and focus photosynthetic active radiation (PAR, 400-700 nm) [De Stefano et al., 2007, De Tommasi et al., 2010], to support photonic pseudo-band gaps [Goessling et al., 2020], and to protect the cell from detrimental ultraviolet radiation (UVR) [Aguirre et al., 2018, De Tommasi et al., 2018]. All these features contribute to diatom high efficiency of sunlight harvesting also where it is not so easily accessible, and have been exploited in several technological fields where light manipulation and control are essential, such as super-resolution [De Tommasi et al., 2014], enhancement of efficiency in dye-sensitized solar cells (DSSCs) [Bandara et al., 2020], plasmonics and surface enhanced Raman spectroscopy [Managò et al., 2018], optical sensing and biosensing [Rogato and De Tommasi, 2020], and random lasing [Lamastra et al., 2014], to name a few.

Here, our aim is to describe the journey of sunlight through the atmosphere, the water bodies, the intricate silica matrix of the frustule, and finally illustrate its interaction with the photosynthetic machinery of the cell. We will mainly focus on the mathematical depiction of all the involved phenomena, in particular analyzing the equations which rule underwater light propagation, describing frustule morphology and shape by means of innovative geometrical approaches based on Gielis superformula [Gielis, 2003b], introducing the main numerical methods used to describe light propagation through the frustule seen as a periodic dielectric medium, and deepening the behavior of plastids seen as efficient antennas.

2 The underwater light field

Before analyzing the underwater optical field and its mathematical description, we will briefly summarize the main characteristics of the solar radiation incident on Earth's surface and transmitted by the air-water interface. We further consider qualitatively light absorption and scattering in a water body. Finally, the main equation governing underwater light propagation will be illustrated, together with a representative computational method aimed at its solution.

2.1 The travel of light from the Sun into water bodies

Light irradiated by the Sun and propagating through atmosphere is partially scattered by air molecules and dust particles and absorbed by water vapour, oxygen, ozone and carbon dioxide, among others [Barlow, 1963]. Being much smaller than the wavelength of solar radiation and according to Rayleigh's law, air molecules mostly scatter radiation in the visible and ultraviolet (UV) range of the electromagnetic spectrum, while dust particles obey to Mie scattering which is not so strictly dependent on wavelength and is predominant in forward direction. A higher proportion of infrared radiation in comparison to photosynthetic active radiation (PAR) is absorbed by water vapours, thus PAR represents the most abundant solar radiation which reaches Earth's surface [Baker and Frouin, 1987]. Taking into account also the contribution of clouds, it has been estimated that 34% of the incoming solar radiation incident on the northern hemisphere over a year is reflected to space by atmosphere (25% reflected by the clouds and 9% scattered out to space by other constituents of the atmosphere); another 19% is absorbed (10% within the clouds and 9% by other components) [Gates, 1963].

The amount of solar radiation reflected back to the atmosphere at the air-water interface depends on the zenith angle of the incident light in air. In first approximation, in particular considering a flat water surface and unpolarized incident light, it can be simply derived from the well-known Fresnel equation [Born and Wolf, 2013]:

$$r = \frac{1}{2}\frac{\sin^2(\theta_a - \theta_w)}{\sin^2(\theta_a + \theta_w)} + \frac{1}{2}\frac{\tan^2(\theta_a - \theta_w)}{\tan^2(\theta_a + \theta_w)} \tag{1}$$

where r stands for reflectance and θ_a and θ_w stand for the zenith angle of incident light in air and the angle to the downward vertical of the transmitted light in water, respectively. When not considering absorption and scattering events, conservation of energy requires that the sum of the reflected and transmitted energy equals the incident energy, thus the quantity $t = 1 - r$ allows evaluating, in first approximation, the amount of light penetrating in the water body. Actually, reflectance is partially reduced by roughening of water surface induced by wind [Austin, 1974] and slightly increased by the formation of whitecaps [Whitlock et al., 1982]. The unreflected portion of an incident light beam is

refracted by water according to Snell's law [Born and Wolf, 2013]:

$$\frac{\sin\theta_a}{\sin\theta_w} = \frac{n_w}{n_a} \tag{2}$$

with n_w and n_a refractive indices of water and air, respectively. Even though the refractive index of water is a function of temperature, salt content and wavelength of incoming radiation, for most practical analyses $\frac{n_w}{n_a}$ ratio can be considered equal to 1.33 for PAR radiation and at normal ambient temperatures. Taking into account this value, it can be derived that most of the light transmitted by water is refracted at an angle θ_w comprised between 0° and 49°. On the other side, considering the case of light propagating upward from water to air at an angle greater than 49°, total internal reflection takes place and all the light is reflected back by the water-air interface.

In general, diffusion of underwater light is enhanced by an increase in wind speed as expressed by the following equations, empirically derived by Cox and Munk [1954] starting from aerial data and the observation of Sun glittering patterns:

$$\sigma_u^2 = 0.003 \cdot U \pm 0.004 \tag{3}$$

$$\sigma_c^2 = 0.003 + 0.002 \cdot U \pm 0.002 \tag{4}$$

with σ_u^2 and σ_c^2 mean square slopes of the waves measured in parallel and cross directions of the wind, respectively, and U wind speed above the water surface.

When light passes through a medium, a certain fraction of it is attenuated whenever absorption or scattering events take place. Transmittance T through a homogeneous medium follows the well-known Lambert-Beer law:

$$T = \exp(-cl) \tag{5}$$

with c total attenuation coefficient taking into account the probability of a photon to be absorbed or scattered after a path length l. Pure water is basically transparent for wavelengths below 550 nm, while absorption starts to be significant in red and mainly in infrared regions of the spectrum, where the roto-vibrational bands, combination bands and overtone bands of water are located [Hill et al., 2016]. Salts present in seawater such as nitrates and bromides contribute to absorption only for wavelengths below 250 nm [Ogura and Hanya, 1966]. A natural source of light absorption, mainly in UV and blue regions, is given by dissolved organic matter originating from plant tissue decomposition (known as *humic substances*). It is estimated that at least 10% of the humic material present in ocean waters is terrestrially derived from river discharges [Meyers-Schulte and Hedges, 1986]. Absorption in UV-blue spectral range is also partially ascribable to inanimate particulate matter (known as *tripton*). Phytoplankton contribute to total absorption of natural waters both in visible spectral range (mainly due to clorophylls, carotenoids and biliproteins) and in near UV (due to the presence of UV-absorbing pigments such as *mycosporine-like amino acids*, MAAs) [Kirk, 1994]. Solar radiation penetrating in a water

body is thus progressively depleted in those spectral regions where the medium mostly absorbs. In clear oceanic waters most of the visible light at depths below ~ 15 m is comprised in the blue-green spectral range (400-550 nm) and peaked in the blue region (440-490 nm) , while UVB radiation has been detected in depths down to 60-70 m [De Tommasi et al., 2018]. In turbid waters characterized by high levels of humic substances, blue light is rapidly removed within shallow depths and the available irradiance often results peaked around 580 nm (yellow) [Kirk, 1994].

In general, the absorption coefficient a of a medium can be defined starting from the effective *absorption cross section* σ_a (which quantifies the probability of the absorption process) as:

$$a = \rho_a \sigma_a \tag{6}$$

with ρ_a volume density of the absorbing particles.

Vertical penetration of light into a water body is also obstructed by scattering, which increases the total path length of propagating radiation and raises the probability of photons to be absorbed by one of the components of the medium. Scattering events can originate from interaction of light with localized microscopic fluctuations of density in the medium. These inhomogeneities can be regarded as induced dipoles which emit radiation at the same frequency of the exciting one. In this case the angular distribution of scattered light is analogous to that given by Rayleigh theory for gases, as well as the wavelength dependence ($\propto \lambda^{-4}$). When the scattering centers are bigger than the wavelength of light (as in the case of mineral particles, phytoplankton, bacteria, dead cells and fragment of cells), Mie theory of scattering has to be taken into account. Instead of considering the scattering centers as single oscillating dipoles, in Mie theory the scattering particle is modeled as the location of the additive contribution of a series of electrical and magnetic multipoles. In this case most of the scattered radiation takes place in forward direction and generally at small angles respect to the propagation axis. In analogy with absorption, the scattering coefficient b can be defined as:

$$b = \rho_s \sigma_s \tag{7}$$

with ρ_s volume density of the scattering particles in the medium and σ_s effective scattering cross-section (quantifying the probability of a scattering event). Referring to Eq.5, total attenuation coefficient c can be thus expressed by $c = a + b$.

2.2 Numerical computation of the underwater optical field

In order to compute the underwater optical field, we have to find solutions to the *radiative transfer equation*, which, in its time-independent, monochromatic and one-dimensional form can be written as [Mobley et al., 1993] (see Table 1

Symbol	Units	Definition
θ	deg	Polar angle of photon travel
ϕ	deg	Azimuthal angle of photon travel
z	m	Depth (defined positive downward)
τ	-	Optical depth (positive downward), $\tau \equiv \int_0^z c(z)d(z)$
L	W m^{-2} sr^{-1} nm^{-1}	Unpolarized spectral radiance
Ξ	-	Set of all downward and upward directions
β	m^{-1} sr^{-1}	Volume scattering function
$\tilde{\beta}$	sr^{-1}	Scattering phase function, $\tilde{\beta} \equiv \beta/b$
S_{in}	W m^{-2} sr^{-1} nm^{-1}	Internal source of radiance

Table 1: Symbols, units and definitions of the quantities in Eq. 8

for symbols definition):

$$\mu \frac{\partial L(\tau;\theta,\phi)}{\partial \tau} = -L(\tau;\theta,\phi) - \frac{b}{c}(\tau) \iint_{(\theta',\phi')\in\Xi} L(\tau;\theta',\phi') \times \tilde{\beta}(\tau;\theta',\phi' \to \theta,\phi) \sin\theta' d\theta' \, d\phi' + S_{in}(\tau;\theta,\phi) \quad (8)$$

It is worth noticing the dependence of the total attenuation coefficient c by depth z and the consequent definition of the optical depth τ as its integral with respect to distance. The radiance $L = L(\theta,\phi)$ leaving an elemental surface dS at polar angle θ and azimuthal angle ϕ is defined, at a fixed depth z and wavelength λ, as:

$$L(\theta,\phi) = \frac{d^2\Phi}{dS\cos\theta d\Omega} \quad (9)$$

where $\Phi = \frac{\partial Q_e}{\partial t}$ is the radiant flux leaving dS within the elemental solid angle $d\Omega$ and Q_e is the radiant energy. The involved geometry is schematized in Fig. 1.

The scattering phase function $\tilde{\beta}(\theta,\phi)$ appearing in the double integral of Eq.8 gives information on how light incident on an elemental volume is scattered in different directions [Mobley et al., 2002]. It can be derived starting from the volume scattering function $\beta(\theta,\phi)$, which in turn is defined as [Agrawal, 2005]:

$$\beta(\theta,\phi) = dI/[L(\theta,\phi)\cdot dV] \quad (10)$$

i.e. as the radiant intensity ($I = \frac{d\Phi}{d\Omega}$) emanating from an elemental volume dV in a given direction (θ,ϕ) per unit incident radiance L. The scattering phase function can be obtained simply dividing the volume scattering function by the scattering coefficient b, which can be defined, in alternative to Eq. 7 and for a given wavelength λ, as:

$$b = \int_{4\pi} \beta(\theta,\phi)d\Omega = 2\pi \int_0^\pi \beta \sin\theta d\theta \quad (11)$$

where the symmetry of the azimuthal angle ϕ has been taken into account.

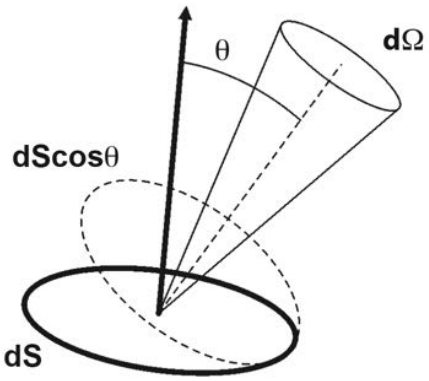

Figure 1: Visual representation of the quantities used in the definition of radiance $L = L(\theta, \phi)$: polar angle defining photon travel (θ), elemental surface (dS), its projection on the direction of propagation of light ($dS\cos\theta$), and elemental solid angle surrounding the same direction ($d\Omega$).

In summary, Eq.8 expresses the conservation of energy of an underwater beam of light: the first term on the right gives the Lambert-Beer loss, the second term is the gain from light scattered from the direction defined by angles (θ', ϕ') into the direction defined by (θ, ϕ), and the third term refers to internal sources of radiance (e.g. bioluminescence). Many numerical models aimed at the solution of Eq. 8 are based on a first partitioning of Ξ, the set of all downward and upward directions, into a grid of so called *quads*, i.e. quadrilateral regions bounded by lines of constant μ and ϕ, plus two polar caps [Mobley et al., 1993], with $\mu \equiv \cos\theta$. In this partitioned domain, the evaluated quantity is the *quad-averaged radiance*:

$$L(\tau; u, v) \equiv \frac{1}{\Omega_{uv}} \iint_{(\mu,\phi)\in Q_{uv}} L(\tau; \mu, \phi) d\mu d\phi \tag{12}$$

where Q_{uv} stands for the uvth quad subtending the solid angle $\Omega_{u,v}$, u labels μ bands and v labels ϕ bands. When applying the integral operator described in Eq.12 to Eq.8, integration over all directions is replaced by summation over all quads and the phase function $\tilde{\beta}(\tau; \mu', \phi' \rightarrow \mu, \phi)$ is replaced by the quad-averaged quantity $\tilde{\beta}(\tau; r, s \rightarrow u, v)$ that specifies the radiance amount scattered from quad Q_{rs} into quad Q_{uv}. The equations for $L(\tau; u, v)$ can be transformed into a set of Riccati differential equations (first-order ordinary differential equations that are quadratic in the unknown function) describing the dependence of reflectance and transmittance functions by depth within the water body. This approach, described in detail in Mobley [1989], allows the modelling of absorption and scattering events as sums of terms representing contributions by pure water, particles, and dissolved substances. Furthermore, reflectance and transmittance of the sea surface from above and below are evaluated making

use of the Monte Carlo simulation of the surface itself, which is resolved into a grid of triangular wave facets characterized by random vertex elevations determined starting from a wave slope-speed spectrum (see for example Eqs. 3 and 4) [Preisendorfer and Mobley, 1986]. The atmospheric radiance incident onto the sea surface can be derived from an analytical model (e.g. a cardioidal distribution) or from a separate atmospheric radiative transfer model. On the other side, the bottom boundary can be schematized as a semi-infinite homogeneous layer of water starting at some depth τ_{max} or an opaque bottom at τ_{max}. In the first case, the bidirectional radiance reflectance properties of the infinite water layer, the asymptotic diffuse attenuation coefficient k_∞, and the asymptotic radiance distribution $L_\infty(\mu)$ can be obtained by an eigenmatrix analysis, as the one introduced by Preisendorfer [1988]. In the second case, a Lambertian surface (i.e. an ideal matte surface characterized by an isotropic luminance) with a given irradiance reflectance is able to describe the reflectance properties of the bottom.

In conclusion, this approach (which represents only one of the possible ways to solve Eq.8), has a strong analytical basis related to the solution of the Riccati differential equations for the retrieval of the radiance L. The only Monte Carlo fluctuations are restricted to the numerical simulation of the sea surface. The computation time is a linear function of depth, thus accurate radiance distributions are obtained for sufficiently high values of τ (typically for $\tau > 10$) [Mobley, 1988].

3 Novel geometrical models for diatoms

3.1 Gielis transformations

Thus far light has travelled through (relatively) isotropic media, with no preferred directions, but when it reaches the diatoms, matters become very different. Most methods in physics and mathematical physics assume isotropy in some sense, but frustules of diatoms have very characteristic shapes, and apart from centric diatoms, they are distinctly anisotropic. In addition, methods borrowed from mathematical physics and differential geometry are local methods, inherited from the pointwise method of determining curvature of curves developed by Newton.

Ultimately the shape of the frustules, the structure of valves and girdles, and the distribution of pores need to be studied via mathematics, with emphasis on geometry, optimization and energy minimization, but the question is whether the methods borrowed from physics are adequate to study living organisms. In particular, there is a need for dedicated geometrical structures, describing living (and non-living) natural shapes into one coherent global framework. Gielis transformations are a recent development that allows one to study biological shapes and phenomena, generalizing Lams superellipses [Gielis, 2003a, Gielis et al., 2005, Gielis, 2017]. Its origin is in the study of plants and organisms, hence it is a scientific method *sui generis*, for what we can observe in our

macroscopic world. In the past five years over 40 000 botanical specimen have been tested, and Gielis transformations and superellipses are found everywhere [Gielis, 2017]. In contrast, circles and ellipses are very rare in biology (centric diatoms may be exceptions to this rule).

This geometrical treatment of diatoms from a global viewpoint, should be integral part of a systems biological approach, coupling insights on form and function to understand genomic and genetic diversity in diatoms, during evolution and development (see Fig. 2). In diatoms this genetic toolbox is known to be very complex with a rich history, and it is thus important to understand form and function, since mathematical and physical laws are prevalent in our universe.

Gielis Transformations are a generalization of the circle (as a constant function) and of the Pythagorean Theorem: indeed, selecting $n_1 = n_2 = n_3 = 2$ and $f(\vartheta) = R = 1$ gives the unit circle and the Pythagorean theorem. Instead of only the classic Euclidean circle, Eq. (13) defines natural shapes at all levels, such as diatoms, starfish, flowers and molluscs. The exponents $n_{1,2,3}$ change the basic polygons defined by the symmetry parameter m. Parameters A and B are scaling parameters. If $A = B$, the basic shape is a circle, but when they differ, the basic shape is an ellipse. Since shape and size parameters are real numbers, a huge diversity and variability can be described in a very compact way:

$$\varrho(\vartheta, f(\vartheta), A, B, m, n_1, n_2, n_3) = \frac{1}{\sqrt[n_1]{\left|(1/A)\cos(m\vartheta/4)\right|^{n_2} + \left|(1/B)\sin(m\vartheta/4)\right|^{n_3}}} \cdot f(\vartheta) \quad (13)$$

In particular, diatoms and their substructures can be described in one coherent framework (Figure 2). With $m = 0$ (circle) radially symmetrical cylindrical frustules can be described, and with increasing m various diatom shapes are modelled. Square shapes have $m = 4$ and benthic diatoms with pennate shapes have bilateral symmetry, defined by $m = 2$. *Stictodiscus* diatoms can be circular but also triangular ($m = 3$) or square. Higher symmetries can be observed in sectorized *Arachnodiscus* or *Cosnicodiscus*. Actually, the parameter m divides the plane into m sectors. Equation (14), a generalization of the sphere for $f(\vartheta, \varphi) = R$ (= the radius of the sphere), can describe the shape of the complete frustule:

$$\varrho(\vartheta, \varphi,\ f(\vartheta, \varphi), A, B, C, m_1, m_2,\ n_1, n_2, n_3, n_4) = \frac{1}{\sqrt[n_1]{\left|\frac{1}{A}\sin(\frac{m_1}{4}\vartheta)\cdot\cos(\frac{m_2}{4}\varphi)\right|^{n_2} + \left|\frac{1}{B}\sin(\frac{m_1}{4}\vartheta)\cdot\sin(\frac{m_2}{4}\varphi)\right|^{n_3} + \left|\frac{1}{C}\cos(\frac{m_1}{4}\vartheta)\right|^{n_4}}} \cdot f(\vartheta, \varphi) \quad (14)$$

It describes the complete frustule and the 3D coordinate planes then correspond to the valvar, radial/transapical and the (per)apical planes in diatoms. The arrangement of the pores in fact provides a very specific coordinate system adapted to the shape, as a natural generalization of classical coordinate systems

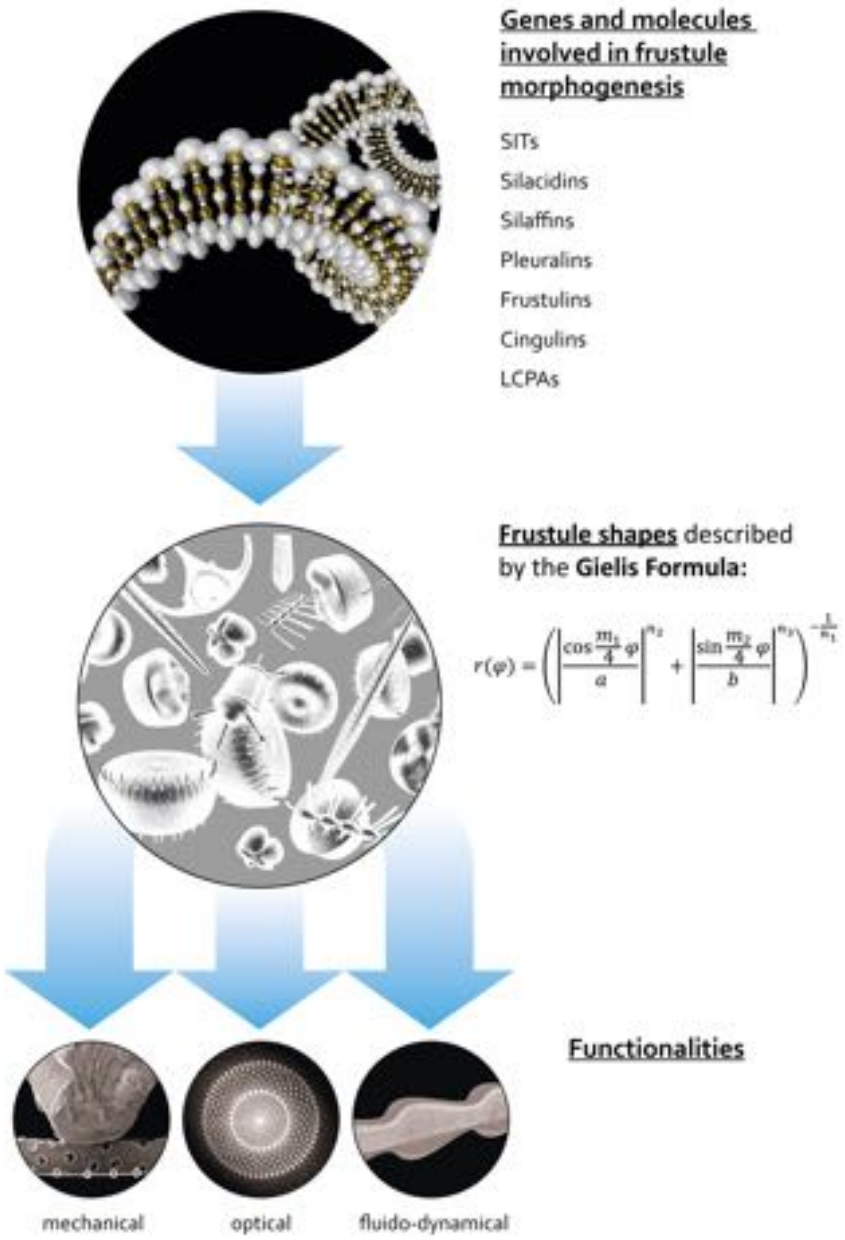

Figure 2: Schematic representation of the connections between frustule morphogenesis, geometry, and physical functions. Reproduced with permission from De Tommasi et al. [2017b].

such as spherical and elliptical coordinates. Using the frustule and the pores as a natural coordinate system should then allow to understand the mathematical physics underlying species specific and environmental-developmental specific distribution of pores. In this way we can also encompass different symmetries encountered in diatoms, and provide for a quantitative measure for qualitative terms such as elliptical or oval, (sub)circular and (sub-) spherical, crescent shapes, lanceolate, clavate, naviculoid, sigmoid and more.

A geometrization of biology, or more generally of nature, based on forms and formation of natural shapes (a geometrical theory of morphogenesis) requires the combination of a uniform description of shapes, coupled to differential equations within a coherent geometrical framework. This uniform description then generates a best adapted coordinate system for both the complete structure and its details.

The proposed uniform description in diatoms can be very effective in the study of global properties, rather than local. Beyond shape description, we have to understand the forces that generate the shapes. The nearly universal principle in the natural sciences is that the equilibrium configuration of a system can be found by minimizing its total energy among all admissible configurations. When considering the surface as interface between two (or more) immiscible materials, the surface geometry is determined by minimizing the surface tension subject to whatever additional constraints are imposed by the environment. There is a canonical equilibrium surface, called the Wulff shape, that can be characterized as the absolute minimizer of the free energy F among all surfaces enclosing the same three-dimensional volume. Diatoms can be considered as Wulff shapes, on which surface stresses act, and they are the "unit spheres" for an anisotropic energy. With Equations (13) and (14), we can study diatoms as Wulff shapes, minimizing certain anisotropic energy functionals [Koiso and Palmer, 2008]. From a geometrical point of view, diatoms are extremely interesting because the overall stable geometrical structure of frustules, costae and other structures, is combined with local optimization of the precise distribution of the pores. This distribution and the diversity make diatoms individually unique; they are the snowflakes of (the liquid state of) water and they are evolutionary very stable solutions.

3.2 Laplace and Fourier revisited

The morphology of diatoms then can be studied in the same way as crystals, snowflakes, or soap films are studied, based on the harmonic function theory. Solutions to boundary value problems can be found in an analytic way, not only computationally. So far analytic Fourier-like solutions were restricted only to a few domains, but can not be extended to a wide range of domains in 2D and 3D, without the need for meshing and finite elements. Analytic Fourier-like solutions to Laplace, Helmholtz and wave equations have been found for various 2D and 3D domains, including shells. Fourier-like refers to analytic solutions combining Fourier series, with special functions of Hankel and Bessel type. The domains or shells are normal with respect to a suitable spherical coordinate system so

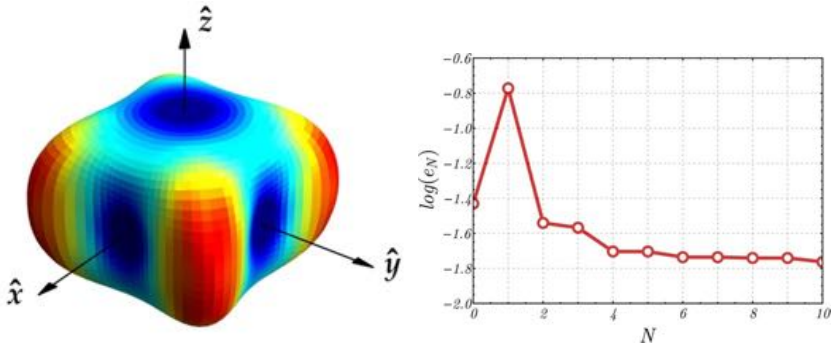

Figure 3: The solution of the Robin problem for the Laplace equation in a shell S with fourfold symmetry in XY direction. Left: Boundary behaviour along the inner shell surface of the partial sum U_N of order $N = 11$. Right: relative boundary error e_N as function of the order N of the truncated spherical harmonic expansion for the super-shaped shell on the left. Reproduced with permission from De Tommasi et al. [2017b].

that the relevant boundary may be regarded as an anisotropically stretched unit circles or spheres. In this way, accurate solutions can be obtained with very low orders of expansions of spherical harmonics. In Caratelli et al. [2009], a number of boundary value problems have been solved in starlike domains, under different boundary conditions. Fig. 3 shows one solution for the Robin problem for the Laplace equation on closed shells with fourfold symmetry in the XY plane), with a cross sectional symmetry observed in *Amphitetras* genus. This method is generally applicable for all 3D shells and the results show that, dependent on the boundary value problem and the boundary conditions chosen, the solutions reflect the way shapes deal with tensions on surfaces. In turn, these tensions are described by the mean curvature H, which is directly related to the Laplacian Δ, due to a Theorem of Beltrami, namely $\Delta = 2H$ for surfaces.

These geometrical methods thus provide a more global view, which can be aligned in the future with existing CAD and Finite Element studies in diatom frustules, but such global geometric view is indispensable if we wish to understand form and function in diatoms.

It is clear that at present we are still far from using this in a complete way, and in studying the fate of photons entering the frustrule and into the protoplast – beyond the glass cage. In Section 4 several classical methods will be presented to simulate light propagation in the frustrule. In Section 5, novel mathematical methods are presented treating the whole diatom as one dielectric complex structure.

4 Going through the wall: simulating light propagation in the frustule

Describing the propagation of light through the intricate but still regular diatom frustules, ultimately means to solve Maxwell equations in presence of a periodic dielectric medium. In their macroscopic formulation, Maxwell equations can be expressed as [Jackson, 1999]:

$$\begin{aligned} \nabla \cdot \mathbf{B} &= 0 \\ \nabla \times \mathbf{E} + \frac{\partial \mathbf{B}}{\partial t} &= 0 \\ \nabla \cdot \mathbf{D} &= \rho \\ \nabla \times \mathbf{H} - \frac{\partial \mathbf{D}}{\partial t} &= \mathbf{J} \end{aligned} \tag{15}$$

where $\mathbf{E}$ and $\mathbf{H}$ are the macroscopic electric and magnetic fields, $\mathbf{D}$ and $\mathbf{B}$ are the displacement and magnetic induction fields and finally ρ and $\mathbf{J}$ stand for free charge and current densities. In absence of sources of light both ρ and $\mathbf{J}$ can be set equal to zero. In linear regime, for isotropic media, and neglecting material dispersion, we have:

$$\begin{aligned} \mathbf{D}(\mathbf{r}) &= \epsilon_0 \epsilon(\mathbf{r}) \mathbf{E}(\mathbf{r}) \\ \mathbf{B}(\mathbf{r}) &= \mu_0 \mu(\mathbf{r}) \mathbf{H}(\mathbf{r}) \simeq \mu_0 \mathbf{H}(\mathbf{r}) \end{aligned} \tag{16}$$

where ϵ_0 stands for vacuum permittivity, ϵ is the dielectric function of the material (purely real and positive for transparent media, like diatom biosilica in visible spectral range), μ_0 is the vacuum permeability and the magnetic permeability $\mu(\mathbf{r})$ is very close to unity for most dielectric materials (thus the refractive index n equals $\sqrt{\epsilon\mu} \simeq \sqrt{\epsilon}$). With all these assumptions, Maxwell equations can be rewritten as follows:

$$\begin{aligned} \nabla \cdot \mathbf{H}(\mathbf{r}, t) &= 0 \\ \nabla \times \mathbf{E}(\mathbf{r}, t) + \mu_0 \frac{\partial \mathbf{H}(\mathbf{r}, t)}{\partial t} &= 0 \\ \nabla \cdot [\epsilon(\mathbf{r}) \mathbf{E}(\mathbf{r}, t)] &= 0 \\ \nabla \times \mathbf{H}(\mathbf{r}, t) - \epsilon_0 \epsilon(\mathbf{r}) \frac{\partial \mathbf{E}(\mathbf{r}, t)}{\partial t} &= 0 \end{aligned} \tag{17}$$

Exploiting the linearity of Maxwell equations, we can separate the time dependence from the spatial dependence by expanding the fields into a set of harmonic modes:

$$\begin{aligned} \mathbf{H}(\mathbf{r}, t) &= \mathbf{H}(\mathbf{r}) e^{-i\omega t} \\ \mathbf{E}(\mathbf{r}, t) &= \mathbf{E}(\mathbf{r}) e^{-i\omega t} \end{aligned} \tag{18}$$

We are thus considering field patterns that vary sinusoidally with time at a frequency ω, which is useful since any solution of the Maxwell equations can

be expressed as a combination of harmonic modes. Inserting the equations 18 in 17 we obtain:

$$\begin{aligned} \nabla \cdot \mathbf{H}(\mathbf{r}) &= 0 \\ \nabla \cdot [\epsilon(\mathbf{r})\mathbf{E}(\mathbf{r})] &= 0 \\ \nabla \times \mathbf{E}(\mathbf{r}) - i\omega\mu_0\mathbf{H}(\mathbf{r}) &= 0 \\ \nabla \times \mathbf{H}(\mathbf{r}) + i\omega\epsilon_0\epsilon(\mathbf{r})\mathbf{E}(\mathbf{r}) &= 0 \end{aligned} \tag{19}$$

The first two equations express the transversality of the electromagnetic waves, while a rearrangement of the last two equations leads to:

$$\nabla \times \left(\frac{1}{\epsilon(\mathbf{r})} \nabla \times \mathbf{H}(\mathbf{r}) \right) = \left(\frac{\omega}{c} \right)^2 \mathbf{H}(\mathbf{r}) \tag{20}$$

which is known as the *master equation* ($c = 1/\sqrt{\epsilon_0\mu_0}$ stands for the vacuum speed of light). Thus, for a given structure characterized by the dielectric function $\epsilon(\mathbf{r})$ (in our case the three-dimensional structure of the diatom frustule), describing how the optical field interacts with it means to solve the master equation to find the modes $\mathbf{H}(\mathbf{r})$ and the corresponding frequencies. The electric fields $\mathbf{E}(\mathbf{r})$ can be finally retrieved by the last equation in 19. Identifying the left side of Eq.20 with a differential operator $\hat{\Theta}$ allows expressing the master equation as an eigenvalue problem:

$$\hat{\Theta}\mathbf{H}(\mathbf{r}) = \left(\frac{\omega}{c} \right)^2 \mathbf{H}(\mathbf{r}) \tag{21}$$

Let's consider a dielectric structure which is periodic in three-dimensions (similar observations can be conducted for one- and two-dimensional systems), i.e. which is invariant under translations through a *lattice vector* $\mathbf{R} = l\mathbf{a_1} + m\mathbf{a_2} + n\mathbf{a_3}$, where $(\mathbf{a_1}, \mathbf{a_2}, \mathbf{a_3})$ are the *primitive lattice vectors* and l, m, and n are integers (in other words we can say that $\mathbf{a_1}$, $\mathbf{a_2}$, and $\mathbf{a_3}$ *span* the space of lattice vectors). The *primitive reciprocal lattice vectors* $(\mathbf{b_1}, \mathbf{b_2}, \mathbf{b_3})$, defined as

$$\mathbf{a_i} \cdot \mathbf{b_j} = 2\pi\delta_{ij} \tag{22}$$

span the so-called *reciprocal lattice*. In this scenario the eigenvectors of $\hat{\Theta}$ corresponding to eigenfrequencies $\omega(\mathbf{k})$ are the *Bloch states*:

$$\mathbf{H_k}(\mathbf{r}) = e^{i\mathbf{k}\cdot\mathbf{r}}\mathbf{u_k}(\mathbf{r}) \tag{23}$$

where $\mathbf{k} = k_1\mathbf{b_1} + k_2\mathbf{b_2} + k_3\mathbf{b_3}$ is the *Bloch wave vector* (with k_1, k_2, and k_3 integer numbers) and $\mathbf{u_k}(\mathbf{r}) = \mathbf{u_k}(\mathbf{r} + \mathbf{R})$ is a periodic function on the lattice. In other words, the eigensolutions of Eq. 21 can be expressed as a product of plane waves and lattice periodic functions (*Bloch-Floquet theorem*). The region of non-redundant values of $\mathbf{k}$ (corresponding to identical Bloch states) in the reciprocal lattice is known as the (first) *Brillouin zone*[1]. It can be easily shown

[1]For more details on the properties of the reciprocal lattice and the Brillouin zone it can be useful to consult a solid-state physics handbook such as Kittel et al. [1996], since the mathematical formalism of lattices is the same.

that inserting the Bloch state described by 23 in the master equation 20 leads to the following eigenvalue problem:

$$\hat{\Theta}_{\mathbf{k}}\mathbf{u}_{\mathbf{k}}(\mathbf{r}) = \left(\frac{\omega(\mathbf{k})}{c}\right)^2 \mathbf{u}_{\mathbf{k}}(\mathbf{r}) \tag{24}$$

where the differential operator $\hat{\Theta}_{\mathbf{k}}$ is defined as:

$$\hat{\Theta}_{\mathbf{k}} = (i\mathbf{k} + \nabla) \times \frac{1}{\epsilon(\mathbf{r})}(i\mathbf{k} + \nabla)\times \tag{25}$$

The mode profiles satisfying the eigenvalue equation 24 are subject to the transversality and periodicity conditions defined by:

$$\begin{aligned} (i\mathbf{k} + \nabla) \cdot \mathbf{u}_{\mathbf{k}} &= 0 \\ \mathbf{u}_{\mathbf{k}}(\mathbf{r}) &= \mathbf{u}_{\mathbf{k}}(\mathbf{r} + \mathbf{R}) \end{aligned} \tag{26}$$

The periodic boundary condition allows us to restrict the eigenvalue problem to a single cell of the lattice. It can be demonstrated [Joannopoulos et al., 2001] that, for each value of $\mathbf{k}$, this leads to a discrete spectrum of eigenvalues that we can label by a band index n. In analogy with the energy band structure of a lattice of atoms subjected to a periodic electric potential $V(\mathbf{r})$, the functions $\omega_n(\mathbf{k})$ describe the frequency of the modes belonging to the nth band of a photonic structure characterized by a periodic refractive index. Photonic crystals (PhCs), in particular, present a geometry and a refractive index contrast respect to the environment such that there exist frequency intervals for which no modes can propagate in the structure. In analogy with the energy band gaps present in semiconductors, these bands are known as *photonic band gaps* (PBGs).

Several species of birds, insects, flora, and protists are provided, as constituent parts of their organisms, with periodic structures at the sub-micron scale acting as photonic crystals [Vukusic and Sambles, 2003, Parker, 2012, Johansen et al., 2017]. This is at the basis of the so called *structural color* [Sun et al., 2013, De Tommasi et al., 2021], which is not due to the presence of pigments absorbing visible radiation but is rather based on spectrally selective reflectance induced by interference processes, which in turn are caused by the periodic spatial arrangement of nanostructured biomaterials. As an example we can mention the flashing, intense blue wings of several species of *Morpho* butterflies [Vukusic et al., 1999, Kinoshita et al., 2002, Giraldo et al., 2016]. Their bright coloration, which is mainly used by males to mark their territory and scare off potential rivals in mating, is mostly due to multilayer interference originating from the *lamellae* of the tree-like ridges observed in the single scales of the wings. In other words, we can claim that the periodically nanostructured wing scales are characterized by a PBG corresponding to the blue spectral range of the visible spectrum.

Nanostructured photonic structures present in nature are not only exploited by animals for intraspecies and interspecies signaling or for camouflage, but also by flora for attracting specific pollinators [Whitney et al., 2009, Moyroud et al.,

2017] and by plants to enhance photosynthetic efficiency [Jacobs et al., 2016]. Nevertheless the most impressive resemblance with artificial PhCs is observed in diatom frustules (see Fig. 4), which allowed Fuhrmann and coworkers to define diatoms as "living photonic crystals" in their pioneering paper in 2004 [Fuhrmann et al., 2004].

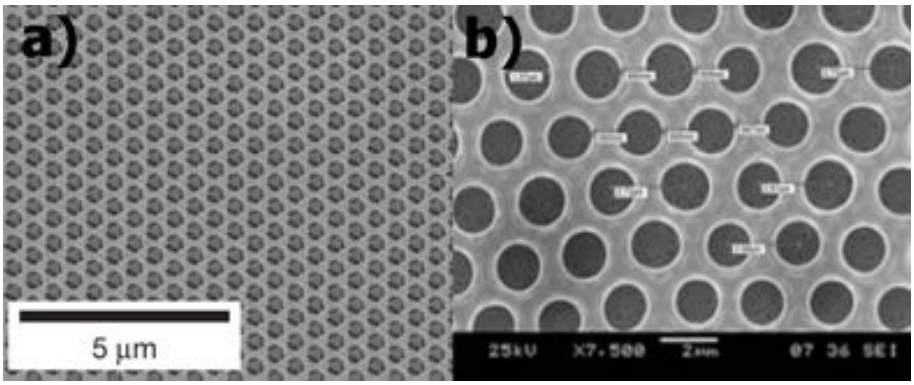

Figure 4: Artificial PhC **(a)** and a detail of a *Coscinodiscus wailesii* valve **(b)**. Reproduced with permission from De Tommasi et al. [2017b].

In the following sections we will briefly review the main numerical methods aimed at the simulation of the electromagnetic field propagation in a periodic photonic structure, both in frequency and time domain and including techniques for PBGs retrieval in a PhC. For every described algorithm, several examples of applications to diatom frustules will be reported.

4.1 Plane Wave Expansion (PWE) method

In order to introduce the Plane Wave Expansion (PWE) method, it can be useful to start from Eq.24 in one dimension[2]. Taking into account the periodicity condition $u_k(x) = u_k(x+a)$, with a period of the lattice, we can express $u_k(x)$ as an infinite sum of sines and cosines, i.e. as a *Fourier series*:

$$u_k(x) = \sum_{n=-\infty}^{\infty} c_n(k) e^{i\frac{2\pi n}{a}x} \tag{27}$$

with:

$$c_n(k) = \frac{1}{a}\int_0^a u_k(x) e^{-i\frac{2\pi n}{a}x} dx \tag{28}$$

The coefficients c_n decay with $|n|$, thus the sum in Eq. 27 can be truncated and reduced to a finite number of N terms. The problem is thus transformed into a set of linear equations for N unknown c_n coefficients. It is worth noticing

[2]For a more detailed discussion on PWE method, refer to Busch and John [1998] and Johnson and Joannopoulos [2001].

that the quantity $\frac{2\pi n}{a}$ in the exponential is a reciprocal lattice vector for a one-dimensional lattice. For a three-dimensional lattice we have, analogously:

$$\mathbf{u_k}(\mathbf{r}) = \sum_{\mathbf{G}} \mathbf{c_G}(\mathbf{k}) e^{i\mathbf{G}\cdot\mathbf{r}} \tag{29}$$
$$\mathbf{c_G} = \frac{1}{V} \int \mathbf{u_k}(\mathbf{r}) e^{-i\mathbf{G}\cdot\mathbf{r}} d^3r$$

where $\mathbf{G} = l'\mathbf{b_1} + m'\mathbf{b_2} + n'\mathbf{b_3}$ is a reciprocal lattice vector and V is the volume of the unit cell. Applying the transversality constraint $(i\mathbf{k} + \nabla) \cdot \mathbf{u_k} = 0$ to the first equation in 29, we obtain:

$$(\mathbf{k} + \mathbf{G}) \cdot \mathbf{c_G} = 0 \tag{30}$$

For each $\mathbf{G}$, we can choose two perpendicular unit vectors $\hat{\mathbf{e}}_{\mathbf{G}}^{(1)}$ and $\hat{\mathbf{e}}_{\mathbf{G}}^{(2)}$ orthogonal to $\mathbf{k} + \mathbf{G}$ such that:

$$\mathbf{c_G} = \mathbf{c_G}^{(1)} \hat{\mathbf{e}}_{\mathbf{G}}^{(1)} + \mathbf{c_G}^{(2)} \hat{\mathbf{e}}_{\mathbf{G}}^{(2)} \tag{31}$$

thus reducing the problem to two unknown coefficients $\mathbf{c_G}^{(1)}$ and $\mathbf{c_G}^{(2)}$ for every $\mathbf{G}$.

We can now substitute $\mathbf{u_k}(\mathbf{r})$ in Eq. 24 with the sum reported in Eq. 29 and then take the Fourier transform of both sides, obtaining the following equation:

$$\sum_{G} \left[-\epsilon^{-1}_{\mathbf{G'}-\mathbf{G}} \cdot (\mathbf{k} + \mathbf{G'}) \times (\mathbf{k} + \mathbf{G}) \times \right] \mathbf{c_G} = \left(\frac{\omega}{c} \right)^2 \mathbf{c_{G'}} \tag{32}$$

$\epsilon^{-1}_{\mathbf{G}}$ standing for the Fourier transform of $\epsilon^{-1}(\mathbf{r})$. We can approximate $\epsilon^{-1}_{\mathbf{G}}$ using the *discrete Fourier transform* (DFT), i.e. replacing it with a finite sum of N terms. After the truncation to a finite set of $\mathbf{G}$ values, the calculation is reduced to a finite matrix eigenequation of the form $Ax = \omega^2 x$. In terms of *time complexity*, the iterative process used to solve the eigenequation generally takes $O(N^2)$ time (i.e. the number of operations of the algorithm scales with N^2). A possible way to reduce time complexity is to make use of the *fast Fourier transform* (FFT) algorithm, which allows computing the multidimensional DFT over N points in $O(N \log N)$ time. We can thus proceed as follows: *i)* we compute the product $(\mathbf{k}+\mathbf{G}) \times \mathbf{c_G}$, which takes $O(N)$ time; *ii)* we calculate the inverse FFT to pass to $\mathbf{r}$ space and multiply by $\epsilon^{-1}(\mathbf{r})$ in $O(N)$ time; finally, *iii)* we pass back to $\mathbf{G}$ space by FFT and perform the cross-product $(\mathbf{k} + \mathbf{G}) \times \mathbf{c_G}$. The overall computation time is $O(N \log N)$ plus $O(N)$ for storage, which improves noticeably the speed of the iteration. Each step of the iteration can be further accelerated by using so called *preconditioners*, i.e. approximate solutions of the eigenproblem. For PWE method an efficient preconditioner is obtained by considering only the diagonal entries of A, which dominate the problem for large values of $|\mathbf{G}|$ [Joannopoulos et al., 2001].

The first application of PWE method to diatom frustules seen as photonic periodic structures was introduced in the aforementioned work by Fuhrmann et al.

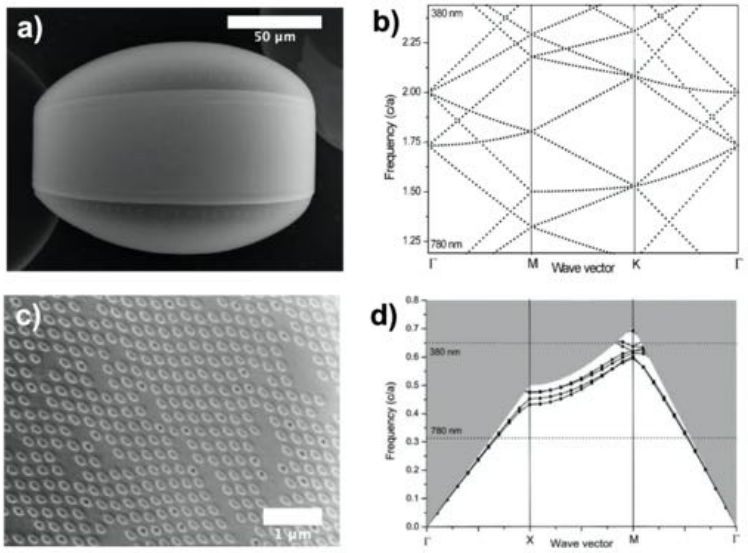

Figure 5: SEM image of a *C. granii* whole frusule (**a**) and two-dimensional band structure of a valve immersed in water as retrieved by effective-index method calculations (**b**). Detail of the girdle (**c**) and relative, numerically reconstructed three-dimensional band structure obtained by PWE method, considering air as surrounding medium (**d**). Reproduced with permission from Fuhrmann et al. [2004].

[2004]. The authors looked at *Coscinodiscus granii* valves and girdles as *photonic crystal slabs*, i.e. photonic structures characterized by a two-dimensional periodicity but a finite thickness. In this case, the properties of a two-dimensional photonic band structure combine with that of a planar waveguide. For the considered species, valves and girdles present an hexagonal and a square pattern of holes, respectively (see Fig. 5). In particular, the valves are characterized by holes with 450 nm radius, a lattice constant of 900-950 nm and a thickness of about 700 nm while the girdles present holes with 90 nm radius, a lattice constant of 250 nm and a thickness which varies in the range of 200-600 nm. PWE was exploited to reconstruct the band structure of the girdle in air (see Fig. 5d) while a two-dimensional calculation based on the effective-index method [Qiu, 2002] was used to investigate the properties of a frustule immersed in water (low refractive index contrast, see Fig. 5b). Let us consider in detail the band diagram reported in Fig. 5d, referring to a girdle with a thickness of 200 nm, a hole radius r/lattice constant a ratio of 0.33, and a refractive index of 1.43. The labels Γ, X, and M indicate special points of the Brillouin zone (the center, the center of an edge, and the center of a face, respectively), while the normalized frequencies of the modes are expressed in units of speed of light divided by the lattice constant. Circles label TE modes (i.e. modes with the electric field parallel to the slab plane) while squares mark TM modes (i.e. modes with the electric field parallel to the holes axis). The shaded area is relative to non-guided modes radiating into air. Let now focus on the spectral range of interest for photosynthesis ($\lambda = 400 - 700$ nm). The frequencies at which the resonances occur and the number of guided modes depend on the shell thickness (in this case 200 nm) and on the refractive index of the surrounding medium. For a frustule immersed in air, the X-resonances are found in gree-yellow spectral range while the M-resonances lie in the blue spectral range. Passing to water as the surrounding environment, the resonating wavelengths are found at 665 nm and 470 nm at the X- and M- points, respectively. In general, in correspondence of these points the group velocity $\frac{\partial \omega}{\partial k}$ is low, implying a long interaction between light and matter. In the case of the valve (5b), the lattice constant is higher than the wavelength of visible light, thus the guided modes lie in infrared region. For visible light, higher order resonances have to be considered which stand above the light line (defined as $\omega(k) = \frac{ck}{\sqrt{\epsilon}}$), thus being partially coupled to radiative modes. This means that the valve can be regarded as a two-dimensional grating coupler of higher order. When immersed in water, as it is the case reported in figure, several resonances are distributed in the visible range. The authors made also calculations on the *penetration depth* associated to the modes supported by the silica walls, starting from the evaluation of the evanescent wave:

$$E(z) = E_0 e^{-\frac{2\pi}{\lambda_0}\sqrt{n_{eff}^2 - n_m^2}} \tag{33}$$

with n_{eff} effective refractive index of the frustule, n_m refractive index of the surrounding medium, λ_0 vacuum wavelength, and z direction perpendicular to the plane of the slab. It is worth noticing how, for small refractive index contrasts (like the one between porous silica and water and/or cytoplasm), the

evanescent wave can reach far into the living cell, letting an efficient optical coupling with the plastids, which have been observed to migrate close to the frustule walls under dim lighting conditions [Furukawa et al., 1998].

PWE was also applied by Yamanaka et al. [2008] in the calculation of the band structure of the inner shell of *Melosira variance* diatom, viewed as a PhC slab characterized by an hexagonal lattice of pores. Simulations have been carried out considering the frustule immersed in air and in water. In both cases, looking at the spectral range between 400 and 500 nm and considering the M-K direction (K indicating the middle of an edge joining two hexagonal faces in the Brillouin zone), the dispersion curves $\omega = \omega(k)$ result parabolic, showing an enhanced interaction between light and the silica shell. One of the possible advantages of this behavior lies in the ability of the frustule to weaken an excess supply of blue light, which would be harmful for the cell because of the inducted production of active oxygen species such as superoxide, hydrogen peroxide, and hydroxyl radical [Baker and Orlandi, 1995].

4.2 Finite Difference Time Domain (FDTD) method

Finite Difference Time Domain (FDTD) method represents the most common computational technique used to numerically solve Maxwell equations in time domain [Joannopoulos et al., 2001], simulating the propagation in time of both the electric and magnetic fields. A detailed description of the algorithm can be found for example in Ref. Taflove and Hagness [2000]. Basically, space and time are divided into a (usually) uniform grid of discrete points and the derivatives present in the Maxwell equations are approximated by finite differences, as the name of the method suggests. The electric fields $\mathbf{E}$ at time t are computed starting from the stored values of the $\mathbf{E}$ fields at time $t - \Delta t$ and from the $\mathbf{H}$ fields at time $t - \Delta t/2$, and vice versa for $\mathbf{H}$ at $t + \Delta t/2$. Like all the time-domain methods, FDTD allows estimating the transmission or reflection of a structure at many frequencies with a single computation, starting from the Fourier transform of its response to a short pulse (broad bandwidth excitation). Frequency eigenvalues of the system, corresponding to resonant or leaky modes, can be retrieved as peaks in the spectrum of the response, while the imposition of Bloch-periodic boundary conditions allows for the computation of band structures. Loss rates can be calculated as easily as resonant frequencies. A separate simulation performed with a narrow-bandwidth source can be used to reconstruct the field pattern corresponding to a specific eigenfrequency. For high spatial resolution simulations, a high temporal resolution is required as well, thus the computational time of a 3D FDTD simulation scales to the fourth power of the resolution.

A precise morphological characterization based on scanning electron microscopy (SEM) allowed Goessling and co-workers [Goessling et al., 2020] to perform FDTD calculations on accurate 3D CAD reconstructions of *C. granii* girdle, which, as we saw in the previous subsection, can be described as a square lattice of cylindrical holes perforating a silica slab (see Fig. 6a,b). These simulations showed, for a girdle immersed in water and considering in-plane propa-

gation, the presence of a so-called *pseudogap* (i.e. a photonic band gap existing only for particular directions of propagation) spectrally located in near infrared (with a central wavelength $\lambda_c \simeq 780$ nm). The pseudogap has been observed also experimentally and undergoes a blue-shift as the incidence angle θ_i increases (see Fig. 6c). A secondary reflectance pattern, due to in-plane diffraction of the modes guided by the girdle, appears in green spectral region for $\theta_i \simeq 50°$. Since both pseudogap and guided modes resonate far from the absorption maxima of chlorophylls, the authors hypothesize that the photonic properties of the girdle evolved in such a way to reduce the interference of photosynthetically not-productive wavelengths with pigment light absorption.

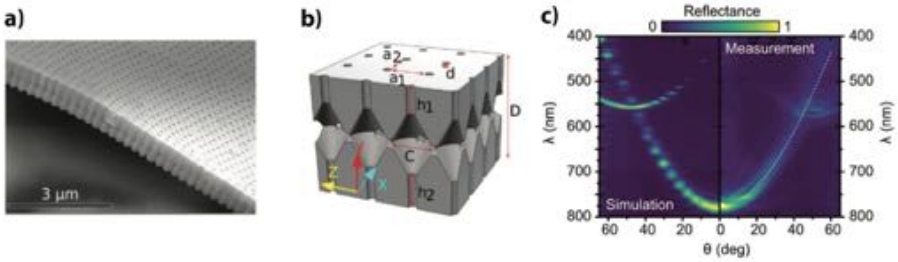

Figure 6: **(a)** Cross-sectional view of a *C. granii* girdle (SEM image). **(b)** 3D CAD recinstruction over four unit cells of the girdle. Numerical values derived by SEM characterization: $a_1 = 285 \pm 5$ nm; $a_2 = 279 \pm 11$ nm; $d = 124 \pm 21$ nm; $h_1 = 225 \pm 21$ nm; $h_2 = 250 \pm 32$ nm; $C = 290 \pm 18$ nm; $D = 745 \pm 43$ nm. **(c)** Reflectance of the girdle immersed in water as a function of incidence angle (for in-plane propagation) and for different wavelengths as retrieved by FDTD simulations (left) and measured by micro-scatterometry (right). Reproduced with permission from Goessling et al. [2020].

In Ref. DMello et al. [2019], the photonic band structure associated to the triangular and square lattice configurations of *Nitzschia filiformis* frustules has been calculated by 3D FDTD, revealing the presence, in both cases, of resonances at symmetry points around 430 and 660 nm respectively, coinciding with the main peaks of absorption of chlorophyll A, one of the chromophores typically found in diatoms. In resonant condition the group velocity lowers, the propagation time within the frustule becomes longer and the probability of light-matter interaction in the proximity of the silica walls, where the chloroplasts lie, increases as well. The resonant photonic behavior of *N. filiformis* shells have been demonstrated also experimentally by means of near-field optical microscopy (SNOM) and correlated atomic force microscopy (AFM) [DMello et al., 2018, 2019].

4.3 Wide-Angle Beam Propagation Method (WA-BPM)

Besides the evaluation of the band structure of a diatom frustule seen as a photonic crystal, it can be useful to study how the light normally impinging on

a valve interacts with its porous matrix and how the transmitted radiation is spatially distributed inside the cell. The typical dimensions of the valve pores are indeed of the same order of magnitude of the visible wavelength, thus giving rise to diffraction. Diffracted light contributions coming from the pores interact with each other by means of interference along the direction of propagation of the field, giving rise to intensity maxima which look like intense hot-spots. This phenomenon has been observed in several centric species [De Stefano et al., 2007, De Tommasi et al., 2010, Di Caprio et al., 2014, Su et al., 2015, Ferrara et al., 2014, Maibohm et al., 2015, Romann et al., 2015] and has been exploited in combination with far-field sub-diffraction techniques in order to obtain a sort of bio-derived super-lens [De Tommasi et al., 2014]. In order to simulate light propagation through a nano-patterned diatom valve, a properly adjusted version of Beam Propagation Method (BPM) can be used. BPM indeed is usually employed in the study of light propagation in waveguides and optical fibers, i.e. in conditions of paraxiality (small angles respect to the optical axis) and of uniformity of refractive index along the direction of propagation of the field. This is not the case of a diatom frustule, where the pores induce diffraction of light (leading to non-paraxial conditions) and where an abrupt variation in the refractive index between the relatively thin valve and the surrounding environment (water or cytoplasm) takes place.

Starting from the Helmholtz equation:

$$\nabla^2 E(\mathbf{r}) + k^2(\mathbf{r}) = 0 \tag{34}$$

with E electric field, $k = nk_0$ wavenumber (with $k_0 = \frac{2\pi}{\lambda}$ wavenumber in free space), and $n = n(x, y, z)$ refractive index spatial distribution, we can write the solution as:

$$E(\mathbf{r}) = E(x, y, z) = U(x, y, z)e^{-ik_r z} \tag{35}$$

The electric field can thus be expressed as the product of a slowly varying envelope factor $U(x, y, z)$ and a rapid varying phase factor $e^{-ik_r z}$, with $k_r = n_r k_0$ reference wavenumber (expressed in terms of the reference refractive index n_r), which takes into account the average phase variation of the field. We are assuming that the considered wave propagates primarily along z (i.e. we are considering, at first, paraxial conditions). We will also suppose, for now, that the amplitude varies slowly along z axis too. Inserting $U(x, y, z)e^{-ik_r z}$ into Eq. 34 we obtain:

$$\frac{\partial^2 U}{\partial z^2} + 2ik_r \frac{\partial U}{\partial z} + \frac{\partial^2 U}{\partial x^2} + \frac{\partial^2 U}{\partial y^2} + (k^2 - k_r^2)U = 0 \tag{36}$$

Making use of the *slowly varying envelope approximation*:

$$\left| \frac{\partial^2 U}{\partial z^2} \right| \ll \left| 2k_r \frac{\partial U}{\partial z} \right| \tag{37}$$

we obtain the basic BPM equation:

$$\frac{\partial U}{\partial z} = \frac{i}{2k_r} \Big[\frac{\partial^2 U}{\partial x^2} + \frac{\partial^2 U}{\partial y^2} + (k^2 - k_r^2)U \Big] \tag{38}$$

Pad order (m,n)	$\mathbf{N_m}$	$\mathbf{D_n}$
(1,0)	$\frac{P}{2}$	1
(1,1)	$\frac{P}{2}$	$1+\frac{P}{4}$
(2,2)	$\frac{P}{2}+\frac{P^2}{4}$	$1+\frac{3P}{4}+\frac{P^2}{16}$
(3,3)	$\frac{P}{2}+\frac{P^2}{2}+\frac{3P^3}{32}$	$1+\frac{5P}{4}+\frac{3P^2}{8}+\frac{P^3}{64}$

Table 2: Low-order Padé approximants expressed in terms of the operator P defined in Eq.40.

Specifying $U(x, y, z)$ at a plane $z = z_0$, we can iterate U along the z-axis using finite differences for the x and y derivatives.

The most popular BPM variant which can take into account non-paraxial conditions (Wide-Angle Beam Propagation Method, WA-BPM), is known as the *multistep Padé-based technique* [Hadley, 1992b,a]. We can denote $\frac{\partial}{\partial z}$ with D, and, consequently, $\frac{\partial^2}{\partial z^2}$ with D^2. Eq. 36 can be now viewed as a quadratic equation to be solved for the differential operator D. This yields to the following solution for a first order equation in z:

$$\frac{\partial U}{\partial z} = ik_r(\sqrt{1+P}-1)U \tag{39}$$

with:

$$P \equiv \frac{1}{k_r^2}\Big(\frac{\partial^2}{\partial x^2}+\frac{\partial^2}{\partial y^2}+(k^2-k_r^2)\Big) \tag{40}$$

Even though it is restricted to forward propagation of the field ($z > 0$), the above equation is exact in that no paraxiality approximation has been introduced. The radical in Eq. 39 can be evaluated by using a Taylor expansion. The first order of the expansion leads to the standard, paraxial BPM, while higher orders lead to more accurate representations of the propagating field. However, expansion via Padé approximants [Hadley, 1992b] is more accurate than Taylor expansion for the same order of terms. This approach leads to the following equation:

$$\frac{\partial U}{\partial z} = ik\frac{N_m(P)}{D_n(P)}U \tag{41}$$

where N_m and D_n are polynomials in the operator P, and (m, n) is the order of approximation. Some of their low-order values are reported in Table 2.

WA-BPM has been applied with success to *Coscinodiscus wailesii* [De Tommasi et al., 2010, 2018] and *Arachnoidiscus* sp. [Ferrara et al., 2014]. In Fig. 7 both experimental and numerical results are reported for a valve of *Arachnoidiscus* sp. immersed in air and illuminated by red radiation ($\lambda = 640$ nm). A CAD

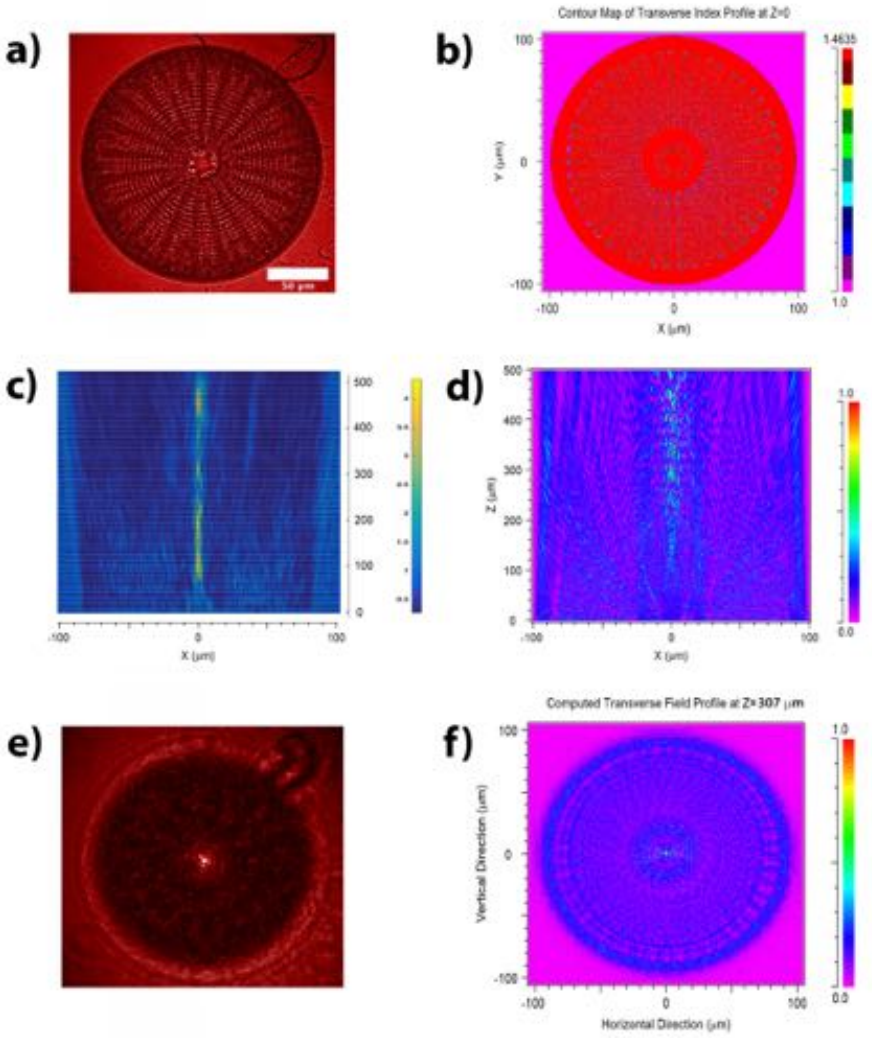

Figure 7: **(a)**: Single valve of an *Arachnoidiscus* sp. diatom illuminated by radiation at $\lambda = 640$ nm; **(b)**: refractive index map (XY plane) of the valve immersed in air retrieved from a SEM characterization of the frustule; **(c)**: experimental transmitted intensity in XZ plane; **(d)**: transmitted intensity in XZ plane as evaluated by WA-BPM; **(e)**: hot-spot acquired at $z = 320$ μm; **(f)**: transmitted intensity evaluated by WA-BPM in XY plane at $z = 307$ μm.

of the valve has been obtained by a SEM morphological characterization of the frustule. In particular, the gray-scale SEM image of the valve has been converted in a binary image, so to obtain a refractive index map which has been then properly extruded (so to obtain a three-dimensional model) and used in simulations. Diffraction caused by the ultrastructure of the valve induces coherent superposition of radiation along the optical axis, giving rise to a train of hot-spots. Even thought the refractive index map is retrieved starting from the image of a real valve (thus giving rise to a more accurate representation respect to simplified valve CADs used in other numerical approaches), the position of the hot-spots as obtained by WA-BPM does not coincide exactly with that observed in experiments, mainly because the CAD used for simulations is basically a perforated disk and does not take into account the actual curvature of the valve. Still the efficient light focusing excerted by the valve is reproduced with a reasonable accuracy. The train of hot-spots extends in a region of hundreds of micrometers. Since, for the considered species, mature frustules are characterized by multiple girdles [Brown, 1933], i.e. the height of the frustule is of the same order of magnitude of the diameter of the valve ($\simeq 200$ μm), it is plausible to hypothesize that part of the confined light lies inside the living cell and that valves contribute to an effective collection of PAR even in environmental conditions where sunlight is not so easily accessible. Furthermore, it has been observed both experimentally and numerically that, in case of UVB radiation (detrimental for DNA mainly through formation of dimeric photoproducts between adjacent pyrimidines), the angle of divergence of diffracted light is such that the train of hot-spots takes place very far from the valve (i.e. outside the living cell) or, for sufficiently low wavelengths, it does not take place at all [Ferrara et al., 2014]. Finally, WA-BPM allows easily evaluating light propagation in whatever environment (e.g. water [De Tommasi et al., 2010] or cytoplasm [De Tommasi et al., 2018]), simply by assigning the right value of refractive index in the algorithm.

4.4 Fast Fourier Transform (FFT) approach

An alternative way to numerically reconstruct the hot-spots which take place beyond a diatom valve when it is irradiated by a plane wave, is to make use of a FFT-based approach within a full diffraction algorithm like the one developed by Delen and Hooker [1998]. Field amplitude $U(x, y, z)$ at a distance $z = L$ from the valve can indeed be expressed as follows:

$$U(x, y, L) = \mathcal{F}^{-1}\{\mathcal{F}\{U(x, y, 0)\}e^{ik_z L}\} \tag{42}$$

where $\mathcal{F}$ and $\mathcal{F}^{-1}$ stand for the Fourier and inverse Fourier transform, respectively, and k_z is the component of the wavevector along the direction of propagation of light. Maibohm et al. [2015] applied this method to reproduce the hot-spots oberved experimentally when a valve of *C. granii* diatom is exposed to coherent (laser) radiation (see Fig. 8). Starting from the quasi-hexagonal symmetry of the valves, a hexagonal pattern of holes has been used as model

for the algorithm, assuming them to be completely transparent to radiation. An absorbing boundary has been implemented in order to avoid undesired reflections.

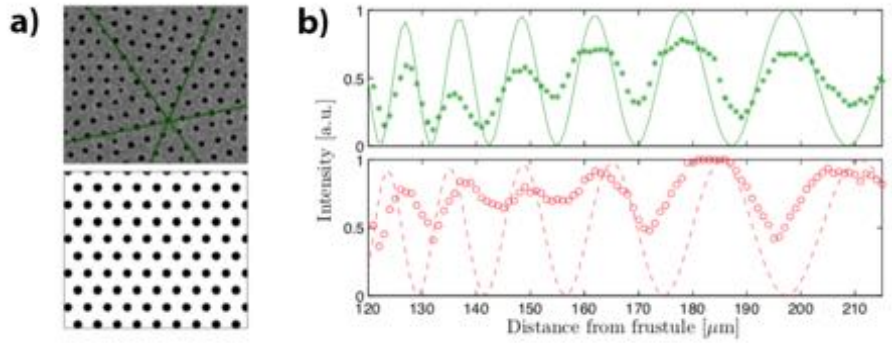

Figure 8: **(a)**: SEM image of a detail of a *C. granii* valve with indication of the hexagonal symmetry of the lattice (top) and corresponding mask used in numerical simulations (bottom). **(b)**: transmitted intensity for $\lambda = 532$ nm (top) and $\lambda = 633$ nm (bottom). Dots represent experimental data, while continuous (top) and dashed (bottom) lines refer to numerical simulations. Reproduced with permission from Maibohm et al. [2015].

5 Fractional calculus for diatoms

The interaction of electromagnetic fields and biological tissues and cells has become a topic of increasing interest for new research activities combining knowledge of electromagnetic theory, modeling, and simulations, physics, material science, cell biology, and medicine [Bia et al., 2016]. The cytoplasm of diatoms contains heterogeneous mixtures of various materials and quantities such as water, ions, membranes, and macromolecules with a broad variety of profiles. Therefore, their interaction with electromagnetic radiation takes place in different relaxation processes including (*i*) reorientation of water and protein-bound water molecules, (*ii*) interfacial polarization arising by the presence of two or more regions with different electrical properties, (*iii*) ionic diffusion, (*iv*) tumbling motion of the protein molecules, and (*v*) relaxations due to the non-spherical shape. These phenomena can cause complex frequency dispersion patterns of permittivity and conductivity [Bia et al., 2016]. Conventional FDTD methods cannot handle such materials, and there is a need for dedicated customized procedures.

Taking in consideration that the study of fractional calculus opens the mind to entirely new branches of applications, we propose to apply such concept to the modeling of diatoms, i.e. as a novel scheme for simulating electromagnetic

pulse propagation in this class of biological structures. Just as fractional exponents may find their way into innumerable equations and applications, the use of fractional order can find practical use in many modern problems. The concept of fractional exponents is an outgrowth of exponents with integer value. In the same way, non-integral order of integration is a generalization of the mathematical operations of differentiation and integration to arbitrary, general, non-integer order. Although it better models the higher complexity by nature, it is still easy to physically represent its meaning. The method is based on the fractional calculus theory and a general series expansion of the permittivity function, dealing with spatial dispersion effects as well. The resulting formulation is explicit, it has a second-order accuracy, and the need for additional storage variables is minimal.

The macroscopic dielectric properties of diatoms are defined by the interaction of the light/electromagnetic energy with the material constituents at microscopic and mesoscopic scale. As a result, the permittivity and electrical conductivity depend on the working frequency. In particular, the characteristics of a general dispersive medium exhibiting multi–relaxation processes can be modeled by using the following relationship [Foster et al., 1986]:

$$\epsilon_r(\omega) = \epsilon_{r_\infty} + \sum_{l=1}^{N} \frac{\Delta\epsilon_{r_l}}{\Gamma_l(i\omega\tau_l)} + \frac{\sigma}{i\omega\epsilon_0}, \tag{43}$$

where $\omega = 2\pi f$ is the angular frequency, ϵ_{r_∞} denotes the asymptotic relative permittivity at high frequency (for $\omega \to +\infty$), $\Delta\epsilon_{r_l}$ is a dimensional constant (also called the dielectric increment in some cases), and $\Gamma_l(i\omega\tau_l)$ is a heuristically derived function depending on the characteristic time τ_l for $l = 1, 2, \ldots, N$, with N being the number of relaxation processes occurring in the considered dielectric material. In (43), σ is the static ionic conductivity, and ϵ_0 denotes the permittivity of free space. Furthermore, we assume that the following condition holds true:

$$\lim_{\omega \to +\infty} |\Gamma_l(i\omega\tau_l)| = +\infty, \tag{44}$$

so to preserve the consistency of the representation.

5.1 Fractional–Calculus–Based Dielectric Dispersion Model

The following approximated fractional power expansion is adopted here:

$$\Gamma_l(i\omega\tau_l) \simeq \sum_{n=0}^{K_l} \chi_{n,l} \left(i\omega\tau_l\right)^{\zeta_{n,l}} = \Gamma_l^{(a)}(i\omega\tau_l, \zeta_{n,l}, \chi_{n,l}), \tag{45}$$

where $\zeta_{n,l}$ and $\chi_{n,l}$ denote suitable real-valued parameters. In particular, in order to avoid model singularities, the exponents $\zeta_{n,l}$ are required to be non–negative.

The parameters K_l, $\zeta_{n,l}$, and $\chi_{n,l}$ can be evaluated, for $l = 1, 2, \ldots, N$, by minimizing the following relative error function over the frequency band of

operation:

$$e_{r_l}(\tau_l, \zeta_{n,l}, \chi_{n,l}) = \sqrt{\frac{\displaystyle\int_{\omega_{\min}}^{\omega_{\max}} \left| \Gamma_l(i\omega\tau_l) - \Gamma_l^{(a)}(i\omega\tau_l, \zeta_{n,l}, \chi_{n,l}) \right|^2 d\omega}{\displaystyle\int_{\omega_{\min}}^{\omega_{\max}} \left| \Gamma_l(i\omega\tau_l) \right|^2 d\omega}}. \tag{46}$$

To this end, the numerical procedure based on the enhanced weighted quantum particle swarm optimization (*EWQPSO*) in [Mescia et al., 2014, Bia et al., 2015] can be conveniently used. The *EWQPSO* technique does not rely on complex operators or require gradient information and, thanks to that, is characterized by reduced computational time, and low memory usage [Giaquinto et al., 2011].

It is worth stressing the fact that the non–linear fitting of the dispersive terms $\Gamma_l(i\omega\tau_l)$ $(l = 1, 2, \ldots, N)$ is carried out in such a way as to prevent outbreaks of the model parameters $\chi_{n,l}$ and $\zeta_{n,l}$ $(n = 0, 1, \ldots, K_l)$ that could lead to instabilities of the time–marching scheme adopted for the numerical solution of Maxwell's equations within the considered dielectric medium. To this end, the search domain is properly constrained, so that the inequality:

$$\mathrm{Im}\left\{ \Gamma_l^{(a)}(i\omega\tau_l, \zeta_{n,l}, \chi_{n,l}) \right\} \geqslant 0, \tag{47}$$

is satisfied for any angular frequency $\omega \in [\omega_{\min}, \omega_{\max}]$ and index $l = 1, 2, \ldots, N$. As known from theory [Hippel, 1994], the enforcement of the inequality (47) is essential to ensure passivity and, in this way, preserve the physical consistency of the approximate model (45).

5.2 Basic Time–Marching Scheme

The evaluation of the electromagnetic field distribution excited by light impinging on a given diatom is here performed by using an extended formulation of the aforementioned finite–difference time–domain (*FDTD*) scheme described in Taflove et al. [2005] and Caratelli et al. [2012], that is useful to model the ohmic losses as well as the multi–relaxation response of media with fractional–power–law frequency dispersion as per (43).

Let us consider a non–magnetic dispersive medium with complex relative permittivity described by (43). Under such assumption, the differential version of the Ampere's law in time domain, within said material, can be written as:

$$\nabla \times \mathbf{H} = \epsilon_0 \epsilon_{r_\infty} \frac{\partial \mathbf{E}}{\partial t} + \sigma \mathbf{E} + \sum_{l=1}^{N} \mathbf{J}_l, \tag{48}$$

with ∂_t denoting the partial derivative operator with respect to time, and where the auxiliary displacement current density terms $\mathbf{J}_l$ $(l = 1, 2, \ldots, N)$ have been introduced. It is straightforward to find out that the k–th term $(1 \leq k \leq N)$ is such to satisfy the equation:

$$\mathcal{D}_t^{(k)} \mathbf{J}_k = \epsilon_0 \Delta\epsilon_{r_k} \frac{\partial \mathbf{E}}{\partial t}, \tag{49}$$

involving the generalized fractional derivative operator:

$$\mathcal{D}_t^{(k)} = \mathcal{F}^{-1}\{\Gamma_k(i\omega\tau_k)\} \simeq \mathcal{F}^{-1}\left\{\Gamma_k^{(a)}(i\omega\tau_k, \zeta_{n,k}, \chi_{n,k})\right\}$$
$$= \sum_{n=0}^{K_k} \chi_{n,k} \tau_k^{\zeta_{n,k}} \mathrm{D}_t^{\zeta_{n,k}}. \tag{50}$$

Upon substituting (49) in (48), and applying a second–order accurate finite–difference scheme, one readily obtains, at the time instant $t = m\Delta t$:

$$(\nabla \times \mathbf{H})|^m - \frac{\epsilon_{r_\infty}}{\Delta\epsilon_{r_k}} \left(\mathcal{D}_t^{(k)} \mathbf{J}_k\right)\Big|^m = \sum_{l=1}^{N} \mathbf{J}_l|^m + \sigma\ \mathbf{E}|^m\,, \tag{51}$$

where the vector terms appearing on the right–hand side of the equation are evaluated by means of the semi–implicit approximation:

$$\left\{ \begin{array}{c} \mathbf{J}_l \\ \mathbf{E} \end{array} \right\}\Big|^m = \frac{1}{2}\left(\left\{ \begin{array}{c} \mathbf{J}_l \\ \mathbf{E} \end{array} \right\}\Big|^{m-\frac{1}{2}} + \left\{ \begin{array}{c} \mathbf{J}_l \\ \mathbf{E} \end{array} \right\}\Big|^{m+\frac{1}{2}} \right). \tag{52}$$

In a similar way, from equation (49) it follows that:

$$\mathbf{E}|^{m+\frac{1}{2}} = \mathbf{E}|^{m-\frac{1}{2}} + \frac{\Delta t}{\epsilon_0 \Delta\epsilon_{r_k}} \left(\mathcal{D}_t^{(k)} \mathbf{J}_k\right)\Big|^m. \tag{53}$$

Let $\nu_{n,k}$ be the integer number such that $\nu_{n,k} - 1 \leqslant \zeta_{n,k} \leqslant \nu_{n,k}$. So, applying the Riemann–Liouville theory based procedure detailed in Mescia et al. [2014] for the finite-difference approximation of the operator $\mathcal{D}_t^{(k)}$ yields, after some mathematical manipulations which are omitted here:

$$\left(\mathcal{D}_t^{(k)} \mathbf{J}_k\right)\Big|^m \simeq \sum_{n=0}^{K_k} \frac{\chi_{n,k}}{(\nu_{n,k} - \zeta_{n,k})!} \left(\frac{\tau_k}{\Delta t}\right)^{\zeta_{n,k}} \sum_{p=0}^{\nu_{n,k}} \left[A_{n,k,p}\ \mathbf{J}_k|^{m-p+\frac{1}{2}} + \sum_{q=1}^{Q_{n,k}} B_{n,k,p,q}\ \mathbf{\Psi}_{n,k,q}|^{m-p} \right], \tag{54}$$

with:

$$\left\{ \begin{array}{c} A_{n,k,p} \\ B_{n,k,p,q} \end{array} \right\} = (-1)^p \binom{\nu_{n,k}}{p} \left\{ \begin{array}{c} \sum_{q=1}^{Q_{n,k}} a_{n,k,q} \\ e^{-b_{n,k,q}} \end{array} \right\}, \tag{55}$$

the positive real–valued coefficients $a_{n,k,q}$ and $b_{n,k,q}$ for $q = 1, 2, \ldots, Q_{n,k}$ being derived through the application of the *EWQPSO* method (see Appendix A) to the non–linear minimization of the function:

$$\Delta_{n,k}(p) = \left| (p+1)^{\nu_{n,k}-\zeta_{n,k}} - p^{\nu_{n,k}-\zeta_{n,k}} - \sum_{q=1}^{Q_{n,k}} a_{n,k,q}\, e^{-b_{n,k,q}p} \right|, \tag{56}$$

depending on the integer index p. In (54), $\boldsymbol{\Psi}_{n,k,q}$ denotes the auxiliary current density vector defined by the following recursion formula:

$$\boldsymbol{\Psi}_{n,k,q}|^{m} = \begin{cases} a_{n,k,q}\, \mathbf{J}_k|^{m-\frac{1}{2}} + e^{-b_{n,k,q}}\, \boldsymbol{\Psi}_{n,k,q}|^{m-1}, & m \geqslant 1, \\ 0, & m \leqslant 0. \end{cases} \tag{57}$$

Finally, by combining (51) with (52), (53), (54), one can readily obtain:

$$\left[\frac{1}{2} + \left(\epsilon_{r_\infty} + \frac{\sigma \Delta t}{2\epsilon_0}\right) \frac{C_k}{\Delta \epsilon_{r_k}}\right] \mathbf{J}_k|^{m+\frac{1}{2}} + \frac{1}{2} \sum_{l=1, l\neq k}^{N} \mathbf{J}_l|^{m+\frac{1}{2}} = \boldsymbol{\eta}_k|^{m}, \tag{58}$$

where:

$$\begin{aligned} \boldsymbol{\eta}_k|^{m} = (\nabla \times \mathbf{H})|^{m} - \sigma \mathbf{E}|^{m-\frac{1}{2}} - \frac{1}{2} \sum_{l=1}^{N} \mathbf{J}_l|^{m-\frac{1}{2}} - \left(\epsilon_{r_\infty} + \frac{\sigma \Delta t}{2\epsilon_0}\right) \\ \cdot \frac{1}{\Delta \epsilon_{r_k}} \sum_{n=0}^{K_k} \frac{\chi_{n,k}}{(\nu_{n,k} - \zeta_{n,k})!} \left(\frac{\tau_k}{\Delta t}\right)^{\zeta_{n,k}} \left[\sum_{p=1}^{\nu_{n,k}} A_{n,k,p}\, \mathbf{J}_k|^{m-p+\frac{1}{2}} \right. \\ \left. + \sum_{p=0}^{\nu_{n,k}} \sum_{q=1}^{Q_{n,k}} B_{n,k,p,q}\, \boldsymbol{\Psi}_{n,k,q}|^{m-p}\right], \end{aligned} \tag{59}$$

and:

$$C_k = \sum_{n=0}^{K_k} A_{n,k,0} \frac{\chi_{n,k}}{\nu_{n,k} - \zeta_{n,k}} \left(\frac{\tau_k}{\Delta t} \right)^{\zeta_{n,k}}, \tag{60}$$

for $k = 1, 2, \ldots, N$. It is apparent from (58) that the evaluation of the displacement current density entails solving a symmetric system of N linear equations, this reflecting the multi–relaxation characteristics of the dielectric material under analysis. As a matter of fact, equations (58) can be recast in the more compact matrix form:

$$\underbrace{\left[\frac{1}{2} \underline{\mathbf{U}} + \left(\epsilon_{r_\infty} + \frac{\sigma \Delta t}{2\epsilon_0} \right) \underline{\mathbf{D}} \right]}_{\underline{\mathbf{T}}} \cdot \mathbf{J}|^{m+\frac{1}{2}} = \boldsymbol{\eta}|^m, \tag{61}$$

with $\underline{\mathbf{U}}$ being the unit matrix of order N, and $\underline{\mathbf{D}} = \mathrm{diag}\{D_1, D_2, \ldots, D_N\}$ the diagonal matrix with nonzero entries $D_k = C_k / \Delta\epsilon_{r_k}$. In (61), $\mathbf{J}|^{m+\frac{1}{2}}$ denotes the vector of the unknown current densities at the time instant $t = \left(m + \frac{1}{2}\right) \Delta t$, namely:

$$\mathbf{J}|^{m+\frac{1}{2}} = \begin{bmatrix} \mathbf{J}_1|^{m+\frac{1}{2}} \\ \mathbf{J}_2|^{m+\frac{1}{2}} \\ \vdots \\ \mathbf{J}_N|^{m+\frac{1}{2}} \end{bmatrix}. \tag{62}$$

Similarly, the column vector $\boldsymbol{\eta}|^m$ is built up by arraying the auxiliary electromagnetic field quantities $\boldsymbol{\eta}_k|^m$ $(k = 1, 2, \ldots, N)$ defined in (59). It is worth noting that the inverse of the coefficient matrix $\underline{\mathbf{T}}$ of the linear system (61) can be conveniently computed only one time before the time–marching scheme is initiated. In this way, the algorithmic implementation of the technique proposed in this research study actually results in a reduced additional computational cost of $O\left(N^2\right)$ floating–point operations useful to determine the solution of (58) as:

$$\mathbf{J}|^{m+\frac{1}{2}} = \underline{\mathbf{T}}^{-1} \cdot \boldsymbol{\eta}|^m. \tag{63}$$

Once the current density terms $\mathbf{J}_l|^{m+\frac{1}{2}}$ $(l = 1, 2, \ldots, N)$ are evaluated, the electric field distribution within the considered dielectric medium can be derived from (48) as:

$$\mathbf{E}|^{m+\frac{1}{2}} = \frac{2\epsilon_0\epsilon_{r_\infty} - \sigma\Delta t}{2\epsilon_0\epsilon_{r_\infty} + \sigma\Delta t} \mathbf{E}|^{m-\frac{1}{2}} + \frac{2\Delta t}{2\epsilon_0\epsilon_{r_\infty} + \sigma\Delta t} \left[(\nabla \times \mathbf{H})|^m - \frac{1}{2} \sum_{l=1}^{N} \left(\mathbf{J}_l|^{m-\frac{1}{2}} + \mathbf{J}_l|^{m+\frac{1}{2}} \right) \right], \tag{64}$$

where judicious use of (52) has been made. Finally, by carrying out a second–order accurate finite–difference approximation of the Faraday's law in the time domain, the following update equation for the magnetic field is readily obtained:

$$\mathbf{H}|^{m+1} = \mathbf{H}|^m - \frac{\Delta t}{\mu_0} (\nabla \times \mathbf{E})|^{m+\frac{1}{2}}, \tag{65}$$

with μ_0 denoting the magnetic permeability of free space.

5.3 Uniaxial Perfectly Matched Layer Boundary Conditions

In order to truncate the *FDTD* computational volume and solve electromagnetic problems involving diatoms in domains with open boundaries, dedicated uniaxial perfectly matched layer (*UPML*) conditions [Gedney, 1996] have to be derived and implemented numerically accounting for the electrical conductivity and the multi–relaxation characteristics of the dielectric material under analysis. To this end, let us first introduce the auxiliary electric field vector $\mathbf{e}$ as:

$$\mathbf{e} = \left(\kappa_x + \frac{\sigma_x}{i\omega\epsilon_0} \right) \mathbf{E}, \tag{66}$$

with κ_x, σ_x denoting the *UPML* material parameters in accordance with the complex coordinate stretching approach Taflove et al. [2005]. Multiplying both sides of (66) by $i\omega$ and transforming into the time domain immediately yields:

$$\frac{\partial \mathbf{E}}{\partial t} = \kappa_x \frac{\partial \mathbf{E}}{\partial t} + \frac{\sigma_x}{\epsilon_0} \mathbf{E}. \tag{67}$$

In this way, it is not difficult to find out that the Ampere's law can be written, within the *UPML* region, as:

$$\nabla \times \mathbf{H} = \epsilon_0 \epsilon_{r_\infty} \frac{\partial \mathbf{E}}{\partial t} + \sigma \mathbf{e} + \sum_{l=1}^{N} \mathbf{j}_l, \tag{68}$$

where the $l-$th displacement current density term ($1 \leq l \leq N$) satisfies the fractional derivative equation:

$$\mathcal{D}_t^{(l)} \mathbf{j}_l = \epsilon_0 \Delta\epsilon_{r_l} \frac{\partial \mathbf{E}}{\partial t}. \tag{69}$$

The discretization of the considered equations on the Yee lattice can be conveniently carried out by adopting the usual leapfrog scheme in time, wherein the loss terms are averaged according to the semi–implicit approximation [see (52)]. Overall, as it can be easily figured out by comparison with (48) and (49), this leads to time–stepping expressions which are formally equivalent to (58) and (64) with the stretched vectors $\mathbf{e}$ and $\mathbf{j}_l$ replacing the quantities $\mathbf{E}$ and $\mathbf{J}_l$, respectively, for $l = 1, 2, \ldots, N$. On the other hand, the electric field update equation directly follows from (67) as:

$$\begin{aligned} \mathbf{E}|^{m+\frac{1}{2}} = \frac{2\epsilon_0\kappa_x - \sigma_x\Delta t}{2\epsilon_0\kappa_x + \sigma_x\Delta t} \, \mathbf{E}|^{m-\frac{1}{2}} + \frac{2\epsilon_0}{2\epsilon_0\kappa_x + \sigma_x\Delta t} \\ \cdot \left(\mathbf{e}|^{m+\frac{1}{2}} - \mathbf{e}|^{m+\frac{1}{2}} \right). \end{aligned} \tag{70}$$

By Fourier–transforming the Faraday's law $\nabla \times \mathbf{E} = -\mu_0 \left(i\omega\kappa_x + \sigma_x/\epsilon_0\right) \mathbf{H}$ and discretizing at the time instance $t = \left(m + \frac{1}{2}\right) \Delta t$, one can readily derive the time–stepping expression for the magnetic field within the *UPML* termination:

$$\mathbf{H}\big|^{m+1} = \frac{2\epsilon_0\kappa_x - \sigma_x \Delta t}{2\epsilon_0\kappa_x + \sigma_x \Delta t}\, \mathbf{H}\big|^{m} - \frac{2Y_0^2 \Delta t}{2\epsilon_0\kappa_x + \sigma_x \Delta t}\, (\nabla \times \mathbf{E})\big|^{m+\frac{1}{2}}\,, \qquad (71)$$

with $Y_0 = \sqrt{\epsilon_0/\mu_0}$ being the wave admittance in free space.

The developed numerical procedure can be used to characterize the electromagnetic behavior of diatoms, modeled as multi-layered dielectric structure, under plane–wave excitation. To this end, the conventional total field/scattered field (*TF/SF*) formulation detailed in Taflove et al. [2005] has been implemented using a sinusoidally time–modulated Gaussian pulse source polarized along the y axis:

$$\mathbf{I}_s(x,t) = \exp\left[-\left(\frac{t - T_c}{T_d}\right)^2\right] \sin\left[2\pi f_e \left(t - T_c\right)\right] \delta(x - x_s)\, \hat{\mathbf{y}}, \qquad (72)$$

with $\delta(\cdot)$ denoting the usual Dirac delta distribution, and where the parameters T_d, $T_c = 4T_d$, f_e have been selected in such a way as to achieve a spectral bandwidth BW.

6 Beyond the glass cage: the fate of light inside the cell

The last leg of the light journey is the cell. The absorbed photons represent sources of information about the environment and environmental signals controlling different physiological, adaptive, and biochemical processes [Depauw et al., 2012]. Pigments are responsible for capturing solar energy. The absorbed light can have three possible fates: generate photochemical reactions leading to production of organic matter; when in excess, can be dissipated as heat [Bailleul et al., 2010] or be emitted back to the environment as fluorescence [Lin et al., 2016]. Diatoms contain two types of pigments involved in light harvesting and photoprotection: chlorophylls and carotenoids (fucoxanthin, β-carotene and the xanthophylls, diatoxanthin, diadinoxanthin, violaxanthin, antheraxanthin, and zeaxanthin). Two forms of chlorophylls are found in diatoms: Chl-a and Chl-c, identified in various algae. Chlorophyll absorbs light in the red (long wavelength) and the blue (short wavelength) portions of the electromagnetic spectrum, which are used in photosynthesis while carotenoids are engaged mainly in photoprotection, with the exception of fucoxanthin that transfers excitation energy very efficiently to Chl-a and plays a major role in the so-called LHC (light-harvesting complex) photosystems [Kuczynska et al., 2015]. The LHC system contains Chl-a and c, and the fucoxanthin (Fx) and is thus referred to as FCP, for fucoxanthin-chlorophyll protein. The pigment composition in FCP reflects the adaptation of diatoms to the blue-green light of the marine environment [Gelzinis et al., 2021]. Moreover, the high amount of the fucoxanthin, that

masks the other carotenoids, is responsible of the characteristic brown color of diatoms [Bertrand, 2010]. However, due to the mixtures of pigments, the absorption spectra of phytoplankton are complex, and it is difficult to quantify the contribution of each pigment. In the last years different studies have been reported in order to find a method that can be successfully used to identify the individual absorption spectra of component pigments such as different derivative analysis and the Gaussian-Lorentzian technique. However, to date, it is still difficult to match the information from the pigments with the absorption spectrum [Aguirre-Gomez et al., 2001].

Like for all living organisms, variation in light/dark cycles due to Earth rotation influences the circadian rhythms of diatoms as well [Annunziata et al., 2019]. In addition, the moon gives off some light of its own and few papers reported its influence on photosynthesis [Raven and Cockell, 2006]. Very recently, Breitler and co-workers [2020] reported for the first time a transcriptomic analysis of the plant *Coffea arabica* under full moonlight conditions. This additional source of photons plays a key role in the light reactions, however, at the moment we can only speculate a possible influence of moonlight on rates of photosynthesis also in diatoms.

Thus, having discussed how the light gets through the water and the cell wall, we now consider what happens inside the cell and which components are involved.

6.1 The diatom chloroplast and its evolution

Unlike plants, green and red algae, the diatom plastid is an evolutionary mosaic, as the one of other photosynthetic members of the stramenopile algae group that are believed to have arisen by secondary endosymbiosis, whereby a non photosynthetic eukaryote acquired a chloroplast by engulfing a photosynthetic eukaryote, probably a red algal endosymbiont [Falkowski et al., 2004]. More recent studies suggest a tertiary endosymbiotic origin, in which a red alga was acquired through secondary endosymbiosis through another algal group which was in turn engulfed by the photosynthetic stramenopile [Dorrell and Bowler, 2017, Dorrell et al., 2017]. Each endosymbiotic event led to new combinations of genes from the hosts and the endosymbionts. The thylakoid membrane inside chloroplasts, capable of forming elaborate networks, harbours the protein complexes that are necessary for the photosynthesis. Plastid genomes have retained a limited number of genes related to the chloroplast function, and other genes have either been lost or transferred to the nuclear genome [Nonoyama et al., 2019]. For this reason, the thylakoids of diatoms are different from the chlorophyte one, with an envelope surrounded by four annular membranes instead of two, and arranged in stacks of three, that are disposed in parallel in a highly ordered manner, where the grana stacking is absent [Levitan et al., 2019]. The four membranes are, from inside out, the inner envelope membrane (iEM), the outer envelope membrane (oEM), the periplasmic membrane (PPM), and the chloroplast endoplasmic reticular membrane (cERM) [Nonoyama et al., 2019] (Fig. 9).

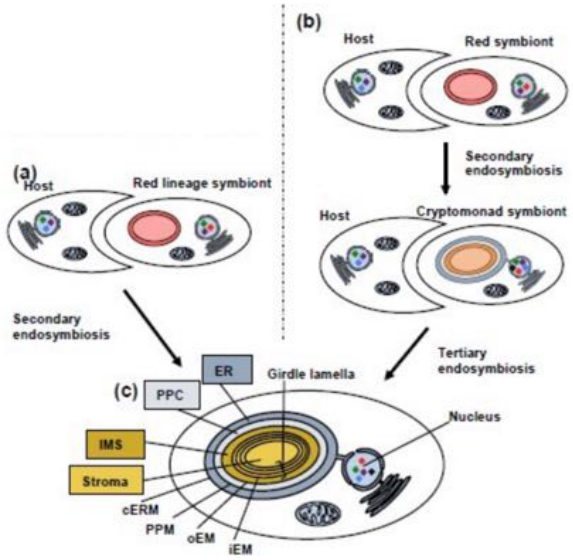

Figure 9: Origin and structure of the diatom chloroplast. The upper panel shows the schematic representation of the secondary (**a**) and tertiary (**b**) endosymbiont hypothesis of diatom evolution. Lower panel (**c**) shows a schematic diagram of the four membranes surrounding the diatom chloroplast. Reproduced with permission from [Nonoyama et al., 2019]. Abbreviations are as follows: cERM; chloroplast endoplasmic reticular membrane; ER, endoplasmic reticulum; iEM, inner envelope membrane; IMS, intermembrane space; oEM, outer envelope membrane; PPC, periplastid compartment; PPM, periplastid membrane.

Depending on the species, diatom plastids can be highly diverse in number and size. Centric diatoms possess plastids ranging from 2 to 3 per cell (like in *Thalassiosira pseudonana*) up to several hundreds (as in *Odontella sinensis*) [Schober et al., 2019]. Interestingly, diatom plastids are characterized by a pronounced motility which strongly depends on both illumination conditions (i.e. photons availability) and spectral content of the impinging radiation. In particular, as already mentioned in section 4.1, in several centric species and for weak illumination conditions, it has been observed a migration of plastids towards frustule walls, well within the region of influence of the evanescent field associated to the modes coupled to valves and girdles (see again Eq. 33). On the opposite, an excess of light intensity induces plastid relocation towards the center of the cell [Furukawa et al., 1998], suggesting the presence of a mechanism useful to nucleus protection from photodamage and/or for an efficient coupling with the hot-spots described in section 4.3. Migration of plastids towards the nucleus is not only triggered by exposure to high light intensity, but it results pronounced also for irradiation in blue spectral range [Shihira-Ishikawa et al., 2007], where one of the maxima of the absorption spectrum of chlorophylls is

located.

6.2 The photosynthetic and electron transport chain

Photosynthesis is a unique process which, in the case of diatoms, takes place with an extremely high efficiency, explaining the ecological success of these microalgae and how they are able to produce approximately 20% of all oxygen on Earth, being directly responsible for 40% of total marine photosynthesis [Field et al., 1998]. Despite distinctions in the architecture of thylakoid membranes, the fundamental machinery responsible for photosynthetic electron transfer is highly conserved in diatoms [Levitan et al., 2019].

Like all oxygenic organisms, light energy is captured by pigments bound to light-harvesting antenna proteins (LHC) that then transfer the energy to the two multi-subunit membrane protein complexes photosystem II (PSII) and PSI, to initiate photochemical reactions (Fig. 10). Recently, thanks to a sophisticated analysis, Flori and colleagues reconstructed the 3D structure of the diatom chloroplast using focused ion beam scanning electron microscopy (FIB-SEM). They demonstrated that, unlike previously thought and as in the case of plants, also in diatoms PSI and PSII are separated and that this separation is necessary to avoid any "short circuits" that would make photosynthesis less effective [Flori et al., 2017]. Even though photosynthetic complexes share fundamental structures, they differ in composition, ratio, and dynamic control of the photosynthetic reactions due to the substantial differences in the light field of marine environments. To cope with the various light environments where different photosynthetic organisms inhabit, different types and numbers of light-harvesting antenna proteins are attached to the PSII core to enhance the light-harvesting and energy-quenching capacities [Falkowski and Chen, 2003, Wang et al., 2020]. Very recently it has been also demonstrated that different diatom classes have various architectures of PSII as an adaptation strategy, whilst a convergent evolution occurred concerning PSI and the overall plastid structure [Arshad et al., 2021].

6.3 The photoprotection mechanism

An excess of light energy may induce damage to the photosynthetic apparatus. A photoprotective response consists in the dissipation of this excess as heat, which occurs in PSII whenever the light absorption exceeds the maximum CO_2 assimilation rate. These processes are at the basis of the so-called non-photochemical quenching (NPQ) and are typical of almost all the photosynthetic eukaryotes, regulating and protecting photosynthesis. The ecological dominance of diatoms also relies on their very efficient photoprotective mechanisms. Diatoms, compared to other photosynthetic organisms, possess a high capacity to dissipate excess light energy as heat through high energy quenching (qE) that, together with the photoinhibitory quenching (qI), can be visualized via the NPQ of Chl-*a* fluorescence [Lepetit et al., 2013, Goss and Lepetit, 2015]. NPQ takes place in the light-harvesting complex antennae (LHC) of PSII. These include

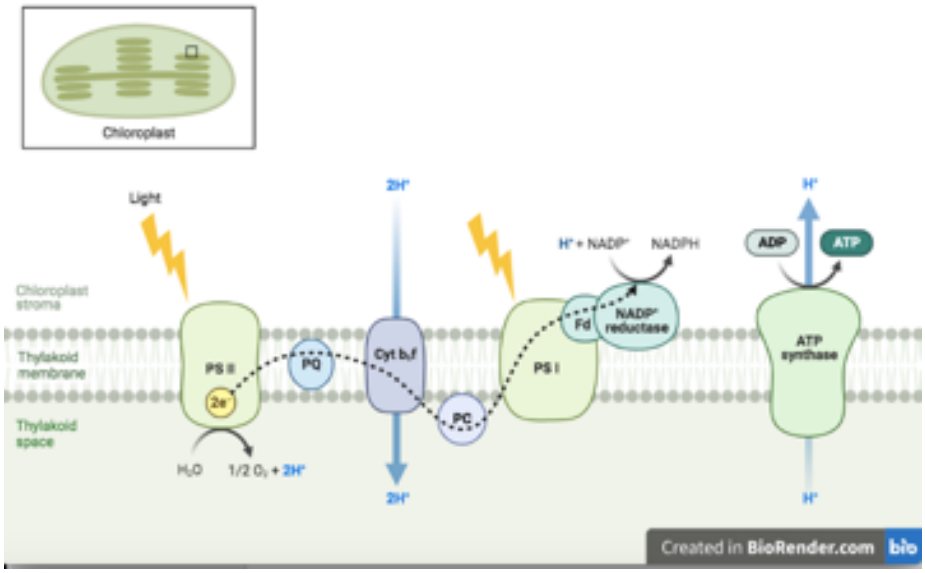

Figure 10: Schematic diagrams of the photosynthetic electron transport chain. Created with BioRender.com

the xanthophyll cycle, which allows diatoms to activate NPQ through the conversion of the accessory pigment diadinoxanthin into diatoxanthin. Along with pigments of the xanthophyll cycle, FCPs and in particular an expanded set of LHCXs family light harvesting proteins also participate in the formation of NPQ to avoid photo-oxidation [Taddei et al., 2016] (Fig. 11). Moreover, it has been recently demonstrated that the excess in chloroplast reducing potential is translocated into the mitochondria and dissipated through respiratory electron transport as an additional photoprotective strategy [Dorrell et al., 2017].

6.4 The Diatom Photoreceptors

Light consists in a spectrum of colours and, as mentioned in section 2, the spectral properties of the underwater light field are very distinct from the terrestrial ones. Light undergoes absorptive and scattering processes throughout the water column, and is affected also by the presence of different photosynthetic organisms [Depauw et al., 2012]. The blue-green (400–500 nm) spectral components dominate in the depth, while the red and infrared wavebands are absorbed by the water, and are present at low intensities, mostly derived from the chlorophyll *a* fluorescence due to the presence of photosynthetic organisms.

Photoreceptors are light-sensing molecules able to perceive the light at specific wavelengths and propagate downstream signal pathways in response, converting the physical light signal into a biochemical signal. They are photon

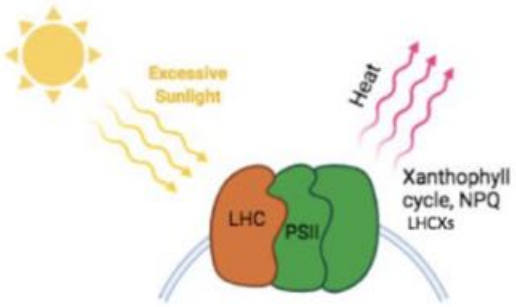

Figure 11: Schematic mechanism of photoprotection. The figure shows the chloroplastic membranes, the light harvesting complexes (LCH) of the photosystem II (PSII) containing pigments that absorbs light for photosynthesis and and the effectors implicated in the non-photochemical quenching of chlorophyll fluorescence (NPQ). Created with BioRender.com

detectors that use visible light to learn about the world around them. These proteins are usually modular in their architecture. They are provided with photoreceptive domains binding chromophores to absorb light signals at specific wavelengths. Chromophores undergo physicochemical and structural changes upon light absorption, which regulate the signal propagation [Depauw et al., 2012] (Fig. 12). In diatoms genome many types of photoreceptors have been identified and partially characterized e.g.: the red light receptors, phytochrome (DPH) [Fortunato et al., 2016], different cryptochromes [Coesel et al., 2009, König et al., 2017] and aureochromes [Mann et al., 2020] for the blue and also heliorhodopsins, a new family of rhodopsins recently discovered [Pushkarev et al., 2018].

6.5 Chlorophyll optical signals for satellite population monitoring

After being absorbed, light can be re-emitted at higher wavelengths through a process called fluorescence. Approximately 2-6% of the solar energy absorbed by chlorophyll is re-emitted as fluorescence [Qiu et al., 2018]. Chlorophyll fluorescence is a detectable signal that provides a way to directly estimate actual photosynthesis from space, reflecting phytoplankton presence and primary productivity. In 2016, Li and colleagues calculated the quantum yield of chlorophyll fluorescence from space by using the images coming from the Moderate Resolution Imaging Spectroradiometer (MODIS) and MEdium Resolution Imaging

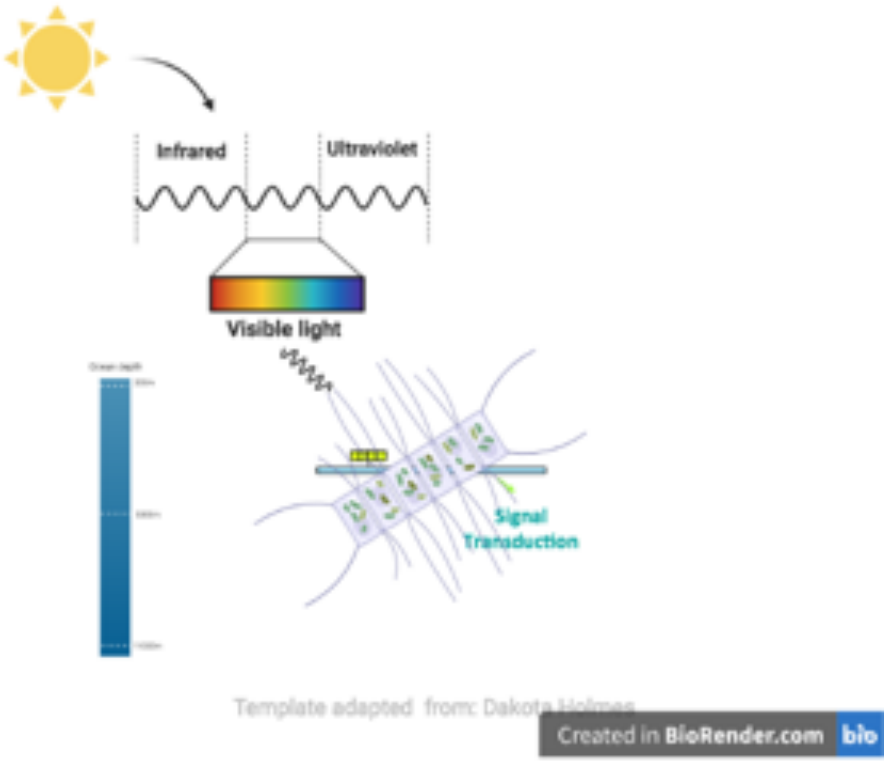

Figure 12: Schematic representation of a simplified view of the phototransduction cascades mediated by photoreceptors. Light in the visible spectrum colors is absorbed by specific photoreceptors which trigger signal transduction cascades that generate physiological responses. Created with BioRender.com

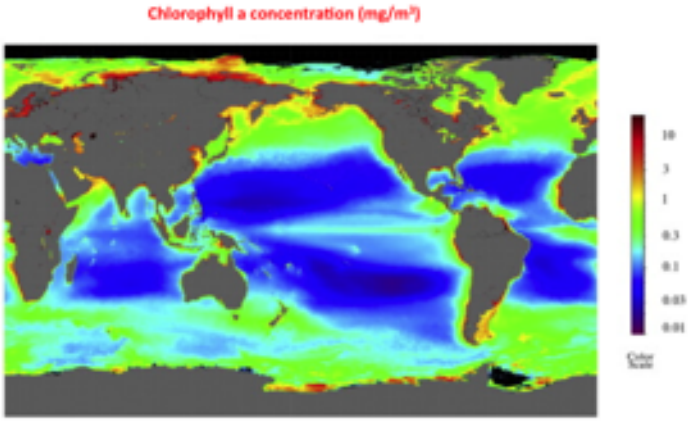

Figure 13: This map shows the average spatial concentration of chlorophyll a in the oceans. Adapted from [Rogato et al., 2015].

Spectrometer (MERIS) satellites, which possess the capability of remotely detecting solar induced chlorophyll fluorescence signals from the global ocean [Li et al., 2016]. Chl-a is routinely derived from satellite-based reflectance using regionally optimized algorithms. The OLCI Neural Network Swarm (ONNS) is an example of bio-geo-optical algorithm for the retrieval of water quality parameters from atmospherically corrected satellite imagery or in situ radiometric measurements. The aim of the development is to provide a single algorithm that is suitable to all natural waters, from oligotrophic ocean waters to very turbid coastal or highly absorbing inland waters. However, total phytoplankton biomass, as indexed by Chl-a concentration, tells only part of the story and differences in optical properties of diatoms can be exploited to develop computational instruments able to distinguish them from other types of phytoplankton. Starting from the observation that diatom populations exhibit much lower specific absorption coefficients than other phytoplankton populations for a given region [Stuart et al., 2000], Sathyendranath and colleagues introduced in 2004 a bio-optical algorithm able to distinguish their contribution and applied it to SeaWiFS data on ocean colour [Sathyendranath et al., 2004]. The SeaWiFS instrument was launched from NASA, by Orbital Sciences Corporation on the OrbView-2 (a.k.a. SeaStar) satellite in August 1997, and collected data from September 1997 until December 2010. SeaWiFS had 8 spectral bands from $\lambda = 412$ nm to $\lambda = 865$ nm. Reflectance at a specific wavelength λ and for a given depth z can be defined as the ratio of upwelling irradiance (E_u) to the downwelling one (E_d):

$$R(\lambda, z) = \frac{E_u(\lambda, z)}{E_d(\lambda, z)} \tag{73}$$

The contribution of elastic scattering to reflectance at sea-surface, $R^E(\lambda, 0)$, is related to total absorption and backscattering coefficients $a(\lambda)$ and $b_b(\lambda)$ by:

$$R^E(\lambda, 0) = r\frac{b_b(\lambda)}{a(\lambda) + b_b(\lambda)} \tag{74}$$

with r proportionality factor. Total absorption coefficient $a(\lambda)$ is given by the sum of the absorption coefficients of pure water (a_w), dissolved organic matter (a_{dom}) and phytoplankton (a_p):

$$a(\lambda) = a_w(\lambda) + a_{dom}(\lambda) + a_p(\lambda) \tag{75}$$

The coefficient a_p can be parametrized as a non-linear function of Chl-a concentration C [Sathyendranath et al., 2001] derived from *in situ* High Performance Liquid Chromatography (HPLC) data:

$$a_p(\lambda) = U(\lambda)\{1 - \exp\left[-S(\lambda)C)\right]\} + Ca_2^*(\lambda) \tag{76}$$

with U [m^{-1}], S [m^3(mg Chl-a)$^{-1}$] and a_2^* [m^2 (mg Chl-a)$^{-1}$] fitting parameters. HPLC data can be indeed used to separate diatom-dominated samples from mixed populations starting from the concentration of Chl-c_3 and fucoxanthin relative to Chl-a (values of Chl-c_3 to Chl-a ratio less than 0.02 and fucoxanthin to Chl-a ratio greater than 0.4 correspond to diatom-dominated regions). In the algorithm, the ratio of reflectances at two wavelengths is always used in order to reduce the effect of any potential errors in the factor r of Eq.74, since the variations in r are independent by the wavelengths used in the ratio. For each pixel of a satellite image we can define the *normalized remote-sensing reflectance* R_{RS}:

$$R_{RS}(\lambda) = \frac{L(0, \lambda)}{E_d(0, \lambda)} \tag{77}$$

where $L(0, \lambda)$ is the upwelling radiance from the sea-surface in the zenith direction at wavelength λ and $E_d(0, \lambda)$ is the downwelling irradiance at the same wavelength. The chlorophyll concentration is first estimated using both the $R_{RS}(510)/R_{RS}(555)$ and $R_{RS}(490)/R_{RS}(670)$ ratios, assuming a diatom population. The difference between the two computed chlorophyll values is then estimated and normalized to the mean of the two values. The operation is repeated assuming a mixed phytoplankton population. The correct model yields smaller differences in the concentrations retrieved using two different waveband pairs if compared to the wrong model. Therefore, each pixel can be assigned to diatom or mixed population, on the basis of the computed normalized differences. In 2018, Kramer and co-workers [Kramer et al., 2018] refined and improved the algorithm through successive re-parameterizations and re-formulations of the absorption and backscattering coefficients, with data collected in different sites.

7 Conclusions

The main analytical models describing the underwater optical field, the essential numerical algorithms for the study of the photonic properties of the diatom seen

as a natural metamaterial and methods for complex EM propagation problems and wave propagation in dispersive materials with multiple relaxation times are described. In the near future, the use of fractional calculus-based methods will be extended to study diatoms and their substructures, in those cases where conventional FDTD techniques fail. In Bia et al. [2016], the plane-wave propagation in a variety of dispersive media has been examined, whereby the comparison between simulated results and those evaluated by using an analytical method based on the Fourier transformation demonstrated the accuracy and effectiveness of the developed FDTD model. The dispersive models might be related further to the absorption spectra of the chromophores described in section 6 and to biosilica dispersion.

Gielis transformations are presented as a unifying geometrical model framework. They allow for great flexibility in modeling and for computational efficiency to be achieved, and have been used for automated detection and determination of diatoms (see Fig. 14) [Seeger, 2021].

Figure 14: Jewels of the Sea. https://maxseeger.de/jewels-of-the-sea. Reproduced with permission of the author.

In presenting a new viewpoint, beyond the classical Euclidean and Riemannian, one enters the realm of Minkowski-Finsler geometry, basically the geometry where the fundamental metric goes beyond the quadratic one. Today, Finsler geometry is the full-sized research theme in mathematics, but it turns out that the simplest of metrics, actually the one proposed by Lam and by Riemann for the infinitesimals, is extremely useful to study natural shapes, in a systems

biology and evolutionary perspective.

Finally, the presented discussion ends up inside the cell, describing all the pigments and the processes involved in light harvesting, photoprotection, and, ultimately, in photosynthesis. Examples of numerical analysis of satellite images for remote sensing of diatom populations are also described, confirming how mathematical modeling not only allows the understanding of the interaction of light with frustules, but also the retrieval of fundamental information about diatom-related primary production.

References

Yogesh C Agrawal. The optical volume scattering function: Temporal and vertical variability in the water column off the new jersey coast. *Limnology and oceanography*, 50(6):1787–1794, 2005.

Luis Ever Aguirre, Liangqi Ouyang, Anders Elfwing, Mikael Hedblom, Angela Wulff, and Olle Inganäs. Diatom frustules protect dna from ultraviolet light. *Scientific reports*, 8(1):1–6, 2018.

R Aguirre-Gomez, AR Weeks, and SR Boxall. The identification of phytoplankton pigments from absorption spectra. *International Journal of Remote Sensing*, 22(2-3):315–338, 2001.

Rossella Annunziata, Andrés Ritter, Antonio Emidio Fortunato, Alessandro Manzotti, Soizic Cheminant-Navarro, Nicolas Agier, Marie JJ Huysman, Per Winge, Atle M Bones, Francois-Yves Bouget, et al. bhlh-pas protein ritmo1 regulates diel biological rhythms in the marine diatom phaeodactylum tricornutum. *Proceedings of the National Academy of Sciences*, 116(26):13137–13142, 2019.

Rameez Arshad, Claudio Calvaruso, Egbert J Boekema, Claudia Büchel, and Roman Kouřil. Revealing the architecture of the photosynthetic apparatus in the diatom *Thalassiosira pseudonana*. *Plant Physiology*, 186(4):21242136, 2021.

RW Austin. The remote sensing of spectral radiance from below the ocean surface. In NG Jerlov and ES Nielsen, editors, *Optical Aspects of Oceanography*. Academic Press, 1974.

B. Bailleul, A. Rogato, A. de Martino, S. Coesel, P. Cardol, C. Bowler, A. Falciatore, and G. Finazzi. LHCX1 an atypical member of the LHCSR protein family, modulates diatoms response to light. *Proc. Natl. Acad. Sci.*, 107: 18214–9, 2010.

C Jacyn Baker and Elizabeth W Orlandi. Active oxygen in plant pathogenesis. *Annual review of phytopathology*, 33(1):299–321, 1995.

Karen S Baker and Robert Frouin. Relation between photosynthetically available radiation and total insolation at the ocean surface under clear skies 1. *Limnology and Oceanography*, 32(6):1370–1377, 1987.

TMWJ Bandara, M Furlani, I Albinsson, Angela Wulff, and B-E Mellander. Diatom frustules enhancing the efficiency of gel polymer electrolyte based dye-sensitized solar cells with multilayer photoelectrodes. *Nanoscale Advances*, 2 (1):199–209, 2020.

HS Barlow. The scientific basis of illuminating engineering. *Physics Bulletin*, 14(1):16, 1963.

Martine Bertrand. Carotenoid biosynthesis in diatoms. *Photosynthesis research*, 106(1):89–102, 2010.

Pietro Bia, Diego Caratelli, Luciano Mescia, R Cicchetti, Guido Maione, and F Prudenzano. A novel fdtd formulation based on fractional derivatives for dispersive havriliak–negami media. *Signal Processing*, 107:312–318, 2015.

Pietro Bia, Luciano Mescia, and Diego Caratelli. Fractional calculus-based modeling of electromagnetic field propagation in arbitrary biological tissue. *Mathematical Problems in Engineering*, 2016, 2016.

Max Born and Emil Wolf. *Principles of optics: electromagnetic theory of propagation, interference and diffraction of light*. Elsevier, 2013.

Jean-Christophe Breitler, Doaa Djerrab, Sophie Leran, Lucile Toniutti, Charlie Guittin, Dany Severac, M Pratlong, Alexis Dereeper, Hervé Etienne, and Benoît Bertrand. Full moonlight-induced circadian clock entrainment in *Coffea arabica*. *BMC Plant Biology*, 20(1):1–11, 2020.

Nicholas Edward Brown. *Arachnoidiscus: An Account of the Genus, Comprising its History, Distribution, Development and Growth of the Frustule, Structure and its Examination and Purpose in Life, and a Key to and Descriptions of All Known Species, Illustrated*. W. Watson, 1933.

Kurt Busch and Sajeev John. Photonic band gap formation in certain self-organizing systems. *Physical Review E*, 58(3):3896, 1998.

Diego Caratelli, Bruna Germano, Johan Gielis, Matthew He, Pierpaolo Natalini, and Paolo Emilio Ricci. Fourier solution for the dirichlet problem for the laplace and helmholtz equations in starlike domains. In *Lecture Notes of Tbilisi International Centre of Mathematics and Informatics*, volume 10. Tbilisi University Press, 2009.

Diego Caratelli, Alessandro Massaro, Roberto Cingolani, and Alexander G. Yarovoy. Accurate time-domain modeling of reconfigurable antenna sensors for non-invasive melanoma skin cancer detection. *IEEE Sensors Journal*, 12 (3):635–643, mar 2012.

Sacha Coesel, Manuela Mangogna, Tomoko Ishikawa, Marc Heijde, Alessandra Rogato, Giovanni Finazzi, Takeshi Todo, Chris Bowler, and Angela Falciatore. Diatom ptcpf1 is a new cryptochrome/photolyase family member with dna repair and transcription regulation activity. *EMBO Reports*, 10(6):655–661, 2009.

Charles Cox and Walter Munk. Measurement of the roughness of the sea surface from photographs of the suns glitter. *Journal of the Optical Society of America*, 44(11):838–850, 1954.

Luca De Stefano, Ilaria Rea, Ivo Rendina, Mario De Stefano, and Luigi Moretti. Lensless light focusing with the centric marine diatom *Coscinodiscus walesii*. *Optics Express*, 15(26):18082–18088, 2007.

E De Tommasi, I Rea, V Mocella, Luigi Moretti, Mario De Stefano, I Rendina, and L De Stefano. Multi-wavelength study of light transmitted through a single marine centric diatom. *Optics Express*, 18(12):12203–12212, 2010.

E De Tommasi, AC De Luca, L Lavanga, P Dardano, M De Stefano, Langella De Stefano, C Langella, I Rendina, K Dholakia, and M Mazilu. Biologically enabled sub-diffractive focusing. *Optics Express*, 22(22):27214–27227, 2014.

E De Tommasi, E Esposito, S Romano, A Crescitelli, V Di Meo, V Mocella, G Zito, and I Rendina. Frontiers of light manipulation in natural, metallic, and dielectric nanostructures. *La Rivista del Nuovo Cimento*, pages 1–68, 2021.

Edoardo De Tommasi, Johan Gielis, and Alessandra Rogato. Diatom frustule morphogenesis and function: a multidisciplinary survey. *Marine Genomics*, 35:1–18, 2017a.

Edoardo De Tommasi, Johan Gielis, and Alessandra Rogato. Diatom frustule morphogenesis and function: a multidisciplinary survey. *Marine genomics*, 35:1–18, 2017b.

Edoardo De Tommasi, Roberta Congestri, Principia Dardano, Anna Chiara De Luca, Stefano Managò, Ilaria Rea, and Mario De Stefano. Uv-shielding and wavelength conversion by centric diatom nanopatterned frustules. *Scientific reports*, 8(1):1–14, 2018.

Nuri Delen and Brian Hooker. Free-space beam propagation between arbitrarily oriented planes based on full diffraction theory: a fast fourier transform approach. *JOSA A*, 15(4):857–867, 1998.

Frauke Angelique Depauw, Alessandra Rogato, Maurizio Ribera dAlcalá, and Angela Falciatore. Exploring the molecular basis of responses to light in marine diatoms. *Journal of Experimental Botany*, 63(4):1575–1591, 2012.

Giuseppe Di Caprio, Giuseppe Coppola, Luca De Stefano, Mario De Stefano, Alessandra Antonucci, Roberta Congestri, and Edoardo De Tommasi. Shedding light on diatom photonics by means of digital holography. *Journal of biophotonics*, 7(5):341–350, 2014.

Richard G Dorrell and Chris Bowler. Secondary plastids of stramenopiles. *Advances in Botanical Research*, 84:57–103, 2017.

Richard G Dorrell, Gillian Gile, Giselle Mccallum, Raphaël Méheust, Eric P Bapteste, Christen M Klinger, Loraine Brillet-Guéguen, Katalina D Freeman, Daniel J Richter, and Chris Bowler. Chimeric origins of ochrophytes and haptophytes revealed through an ancient plastid proteome. *elife*, 6:e23717, 2017.

Yannick DMello, Dan Petrescu, James Skoric, Melissa Campbell, Mark Andrews, and David Plant. Characterization of the photonic response in nitzschia filiformis phytoplankton. In *CLEO: QELS_Fundamental Science*, pages JTh2A–96. Optical Society of America, 2018.

Yannick DMello, Santiago Bernal, James Skoric, Dan Petrescu, Mark Andrews, and David V Plant. Photonic crystal behavior of nitzschia filiformis phytoplankton for chlorophyll a photosynthesis. In *CLEO: QELS_Fundamental Science*, pages JW2A–121. Optical Society of America, 2019.

Steven Emerson and John Hedges. *Chemical oceanography and the marine carbon cycle*. Cambridge University Press, 2008.

Paul G Falkowski and Yi-Bu Chen. Photoacclimation of light harvesting systems in eukaryotic algae. In BR Green and WW Parson, editors, *Light-harvesting antennas in photosynthesis*, pages 423–447. Springer, Dordrecht, 2003.

Paul G Falkowski, Miriam E Katz, Andrew H Knoll, Antonietta Quigg, John A Raven, Oscar Schofield, and FJR Taylor. The evolution of modern eukaryotic phytoplankton. *Science*, 305(5682):354–360, 2004.

Maria Antonietta Ferrara, Principia Dardano, Luca De Stefano, Ilaria Rea, Giuseppe Coppola, Ivo Rendina, Roberta Congestri, Alessandra Antonucci, Mario De Stefano, and Edoardo De Tommasi. Optical properties of diatom nanostructured biosilica in *Arachnoidiscus* sp: micro-optics from mother nature. *PLoS One*, 9(7):e103750, 2014.

Christopher B Field, Michael J Behrenfeld, James T Randerson, and Paul Falkowski. Primary production of the biosphere: integrating terrestrial and oceanic components. *Science*, 281(5374):237–240, 1998.

S Flori, PH Jouneau, B Bailleul, et al. Plastid thylakoid architecture optimizes photosynthesis in diatoms. *Nat. Commun.*, 8:15885, 2017.

Antonio Emidio Fortunato, Marianne Jaubert, Gen Enomoto, Jean-Pierre Bouly, Raffaella Raniello, Michael Thaler, Shruti Malviya, Juliana Silva Bernardes, Fabrice Rappaport, Bernard Gentili, et al. Diatom phytochromes reveal the existence of far-red-light-based sensing in the ocean. *Plant Cell*, 28 (3):616–628, 2016.

Kenneth R Foster, Herman P Schwan, et al. Dielectric properties of tissues. In *CRC Handbook of Biological Effects of Electromagnetic Fields*, pages 27–96. CRC Press, Boca Raton, FL, 1986.

T Fuhrmann, S Landwehr, M El Rharbi-Kucki, and M Sumper. Diatoms as living photonic crystals. *Applied Physics B*, 78(3):257–260, 2004.

T Furukawa, M Watanabe, and I Shihira-Ishikawa. Green-and blue-light-mediated chloroplast migration in the centric diatompleurosira laevis. *Protoplasma*, 203(3-4):214–220, 1998.

David M Gates. Energy exchange in the biosphere. *Soil Science*, 96(1):76, 1963.

S.D. Gedney. An anisotropic perfectly matched layer-absorbing medium for the truncation of FDTD lattices. *IEEE transactions on Antennas and Propagation*, 44(12):1630–1639, 1996.

Andrius Gelzinis, Ramūnas Augulis, Claudia Büchel, Bruno Robert, and Leonas Valkunas. Confronting fcp structure with ultrafast spectroscopy data: evidence for structural variations. *Physical Chemistry Chemical Physics*, 23(2): 806–821, 2021.

A Giaquinto, L Mescia, G Fornarelli, and F Prudenzano. Particle swarm optimization-based approach for accurate evaluation of upconversion parameters in er^{3+}-doped fibers. *Optics Letters*, 36(2):142–144, 2011.

Johan Gielis. *Inventing the circle: The geometry of nature*. Geniaal, 2003a.

Johan Gielis. A generic geometric transformation that unifies a wide range of natural and abstract shapes. *American journal of botany*, 90(3):333–338, 2003b.

Johan Gielis. *The geometrical beauty of plants*. Atlantis Press, Paris, 2017.

Johan Gielis, Stefan Haesen, and Leopold Verstraelen. Universal natural shapes: From the super eggs of Piet Hein to the cosmic egg of Georges Lematre. *Kragujevac Journal of Mathematics*, 28:57–68, 2005.

MA Giraldo, S Yoshioka, C Liu, and DG Stavenga. Coloration mechanisms and phylogeny of morpho butterflies. *Journal of Experimental Biology*, 219(24): 3936–3944, 2016.

Johannes W Goessling, William P Wardley, and Martin Lopez-Garcia. Highly reproducible, bio-based slab photonic crystals grown by diatoms. *Advanced Science*, 7(10):1903726, 2020.

Reimund Goss and Bernard Lepetit. Biodiversity of NPQ. *Journal of Plant Physiology*, 172:13–32, 2015.

G Ronald Hadley. Multistep method for wide-angle beam propagation. *Optics Letters*, 17(24):1743–1745, 1992a.

G Ronald Hadley. Wide-angle beam propagation using padé approximant operators. *Optics Letters*, 17(20):1426–1428, 1992b.

Michelle S Hale and James G Mitchell. Functional morphology of diatom frustule microstructures: hydrodynamic control of brownian particle diffusion and advection. *Aquatic Microbial Ecology*, 24(3):287–295, 2001.

Christian E Hamm, Rudolf Merkel, Olaf Springer, Piotr Jurkojc, Christian Maier, Kathrin Prechtel, and Victor Smetacek. Architecture and material properties of diatom shells provide effective mechanical protection. *Nature*, 421(6925):841–843, 2003.

Christian Hill, Iouli E Gordon, Roman V Kochanov, Lorenzo Barrett, Jonas S Wilzewski, and Laurence S Rothman. Hitranonline: An online interface and the flexible representation of spectroscopic data in the hitran database. *Journal of quantitative spectroscopy and radiative transfer*, 177:4–14, 2016.

AR Von Hippel. *Dielectrics and Waves*. Artech House, Norwood, MA, 1994.

John David Jackson. *Classical electrodynamics*. Wiley, 3rd edition, 1999.

Matthew Jacobs, Martin Lopez-Garcia, O-Phart Phrathep, Tracy Lawson, Ruth Oulton, and Heather M Whitney. Photonic multilayer structure of begonia chloroplasts enhances photosynthetic efficiency. *Nature plants*, 2(11):1–6, 2016.

John D Joannopoulos, Steven G Johnson, Joshua N Winn, and Robert D Meade. Molding the flow of light. *MIT Physics Annual*, pages 32–43, 2001.

Villads Egede Johansen, Olimpia Domitilla Onelli, Lisa Maria Steiner, and Silvia Vignolini. Photonics in nature: from order to disorder. *Functional surfaces in biology III*, pages 53–89, 2017.

Steven G Johnson and John D Joannopoulos. Block-iterative frequency-domain methods for maxwells equations in a planewave basis. *Optics Express*, 8(3): 173–190, 2001.

Shuichi Kinoshita, Shinya Yoshioka, Yasuhiro Fujii, and Naoko Okamoto. Photophysics of structural color in the morpho butterflies. *Forma*, 17(2):103–121, 2002.

John TO Kirk. *Light and photosynthesis in aquatic ecosystems*. Cambridge university press, 1994.

Charles Kittel, Paul McEuen, and Paul McEuen. *Introduction to solid state physics*, volume 8. Wiley New York, 1996.

Miyuki Koiso and Bennett Palmer. Equilibria for anisotropic surface energies and the Gielis formula. *Forma*, 23(1):1–8, 2008.

Sarah König, Matthias Juhas, Stefanie Jäger, Tilman Kottke, and Claudia Büchel. The cryptochromephotolyase protein family in diatoms. *Journal of Plant Physiology*, 217:15–19, 2017.

Sasha J Kramer, Collin S Roesler, and Heidi M Sosik. Bio-optical discrimination of diatoms from other phytoplankton in the surface ocean: Evaluation and refinement of a model for the northwest atlantic. *Remote sensing of environment*, 217:126–143, 2018.

Paulina Kuczynska, Malgorzata Jemiola-Rzeminska, and Kazimierz Strzalka. Photosynthetic pigments in diatoms. *Marine drugs*, 13(9):5847–5881, 2015.

Francesca Romana Lamastra, Roberta De Angelis, Alessandra Antonucci, Damiano Salvatori, Paolo Prosposito, Mauro Casalboni, Roberta Congestri, Sonia Melino, and Francesca Nanni. Polymer composite random lasers based on diatom frustules as scatterers. *RSC Advances*, 4(106):61809–61816, 2014.

Karine Leblanc, Bernard Queguiner, Frederic Diaz, Veronique Cornet, Mónica Michel-Rodriguez, Xavier Durrieu de Madron, Chris Bowler, Shruti Malviya, Melilotus Thyssen, Gérald Grégori, et al. Nanoplanktonic diatoms are globally overlooked but play a role in spring blooms and carbon export. *Nature Communications*, 9(1):1–12, 2018.

Bernard Lepetit, Sabine Sturm, Alessandra Rogato, Ansgar Gruber, Matthias Sachse, Angela Falciatore, Peter G Kroth, and Johann Lavaud. High light acclimation in the secondary plastids containing diatom *Phaeodactylum tricornutum* is triggered by the redox state of the plastoquinone pool. *Plant Physiology*, 161(2):853–865, 2013.

Orly Levitan, Muyuan Chen, Xuyuan Kuang, Kuan Yu Cheong, Jennifer Jiang, Melissa Banal, Nikhita Nambiar, Maxim Y Gorbunov, Steven J Ludtke, Paul G Falkowski, et al. Structural and functional analyses of photosystem II in the marine diatom *Phaeodactylum tricornutum*. *Proceedings of the National Academy of Sciences*, 116(35):17316–17322, 2019.

Wenkai Li, Weidong Guo, Yongkang Xue, Congbin Fu, and Bo Qiu. Sensitivity of a regional climate model to land surface parameterization schemes for east asian summer monsoon simulation. *Climate Dynamics*, 47(7):2293–2308, 2016.

Hanzhi Lin, Fedor I Kuzminov, Jisoo Park, SangHoon Lee, Paul G Falkowski, and Maxim Y Gorbunov. The fate of photons absorbed by phytoplankton in the global ocean. *Science*, 351(6270):264–267, 2016.

Christian Maibohm, Søren Michael Mørk Friis, Marianne Ellegaard, and Karsten Rottwitt. Interference patterns and extinction ratio of the diatom coscinodiscus granii. *Optics Express*, 23(7):9543–9548, 2015.

Stefano Managò, Gianluigi Zito, Alessandra Rogato, Maurizio Casalino, Emanuela Esposito, Anna Chiara De Luca, and Edoardo De Tommasi. Bioderived three-dimensional hierarchical nanostructures as efficient surface-enhanced raman scattering substrates for cell membrane probing. *ACS applied materials & interfaces*, 10(15):12406–12416, 2018.

Marcus Mann, Manuel Serif, Thomas Wrobel, Marion Eisenhut, Shvaita Madhuri, Samantha Flachbart, Andreas PM Weber, Bernard Lepetit, Christian Wilhelm, and Peter G Kroth. The aureochrome photoreceptor ptaureo1a is a highly effective blue light switch in diatoms. *iScience*, 23(11):101730, 2020.

Luciano Mescia, Pietro Bia, and Diego Caratelli. Fractional derivative based fdtd modeling of transient wave propagation in havriliak–negami media. *IEEE Transactions on Microwave Theory and Techniques*, 62(9):1920–1929, 2014.

Kathleen J Meyers-Schulte and John I Hedges. Molecular evidence for a terrestrial component of organic matter dissolved in ocean water. *Nature*, 321 (6065):61–63, 1986.

Curtis D Mobley. A numerical model for the computation of radiance distributions in natural waters with wind-roughened surfaces, part 2: User's guide and code listing. Technical report, Washington Univ Seattle Joint Inst for Study of Atmosphere and Ocean, 1988.

Curtis D Mobley. A numerical model for the computation of radiance distributions in natural waters with wind-roughened surfaces. *Limnology and oceanography*, 34(8):1473–1483, 1989.

Curtis D Mobley, Bernard Gentili, Howard R Gordon, Zhonghai Jin, George W Kattawar, Andre Morel, Phillip Reinersman, Knut Stamnes, and Robert H Stavn. Comparison of numerical models for computing underwater light fields. *Applied Optics*, 32(36):7484–7504, 1993.

Curtis D Mobley, Lydia K Sundman, and Emmanuel Boss. Phase function effects on oceanic light fields. *Applied optics*, 41(6):1035–1050, 2002.

Edwige Moyroud, Tobias Wenzel, Rox Middleton, Paula J Rudall, Hannah Banks, Alison Reed, Greg Mellers, Patrick Killoran, M Murphy Westwood, Ullrich Steiner, et al. Disorder in convergent floral nanostructures enhances signalling to bees. *Nature*, 550(7677):469–474, 2017.

Tomomi Nonoyama, Elena Kazamia, Hermanus Nawaly, Xia Gao, Yoshinori Tsuji, Yusuke Matsuda, Chris Bowler, Tsuyoshi Tanaka, and Richard G Dorrell. Metabolic innovations underpinning the origin and diversification of the diatom chloroplast. *Biomolecules*, 9(8):322, 2019.

N Ogura and T Hanya. Nature of ultra-violet absorption of sea water. *Nature*, 212(5063):758–758, 1966.

AR Parker. Natural photonic structures: an overview. *Optical Biomimetics*, pages 1–20e, 2012.

Rudolph W Preisendorfer. Eigenmatrix representations of radiance distributions in natural waters with wind-roughened surfaces. Technical report, Washington Univ Seattle Joint Inst for Study of Atmosphere and Ocean, 1988.

Rudolph W Preisendorfer and Curtis D Mobley. Albedos and glitter patterns of a wind-roughened sea surface. *Journal of Physical Oceanography*, 16(7): 1293–1316, 1986.

Alina Pushkarev, Keiichi Inoue, Shirley Larom, José Flores-Uribe, Manish Singh, Masae Konno, Sahoko Tomida, Shota Ito, Ryoko Nakamura, Satoshi P Tsunoda, et al. A distinct abundant group of microbial rhodopsins discovered using functional metagenomics. *Nature*, 558(7711):595–599, 2018.

Bo Qiu, Yongkang Xue, Joshua B Fisher, Weidong Guo, Joseph A Berry, and Yongguang Zhang. Satellite chlorophyll fluorescence and soil moisture observations lead to advances in the predictive understanding of global terrestrial coupled carbon-water cycles. *Global Biogeochemical Cycles*, 32(3):360–375, 2018.

Min Qiu. Effective index method for heterostructure-slab-waveguide-based two-dimensional photonic crystals. *Applied physics letters*, 81(7):1163–1165, 2002.

JA Raven and CS Cockell. Influence on photosynthesis of starlight, moonlight, planetlight, and light pollution (reflections on photosynthetically active radiation in the universe). *Astrobiology*, 6(4):668–675, 2006.

Alessandra Rogato and Edoardo De Tommasi. Physical, chemical, and genetic techniques for diatom frustule modification: Applications in nanotechnology. *Applied Sciences*, 10(23):8738, 2020.

Alessandra Rogato, Alberto Amato, Daniele Iudicone, Maurizio Chiurazzi, Maria Immacolata Ferrante, and Maurizio Ribera d'Alcalà. The diatom molecular toolkit to handle nitrogen uptake. *Marine genomics*, 24:95–108, 2015.

J Romann, J-C Valmalette, A Røyset, and M-A Einarsrud. Optical properties of single diatom frustules revealed by confocal microspectroscopy. *Optics letters*, 40(5):740–743, 2015.

Frank Eric Round, Richard M Crawford, and David G Mann. *Diatoms: biology and morphology of the genera*. Cambridge university press, 1990.

S Sathyendranath, G Cota, V Stuart, H Maass, and T Platt. Remote sensing of phytoplankton pigments: a comparison of empirical and theoretical approaches. *International Journal of Remote Sensing*, 22(2-3):249–273, 2001.

Shubha Sathyendranath, Louisa Watts, Emmanuel Devred, Trevor Platt, Carla Caverhill, and Heidi Maass. Discrimination of diatoms from other phytoplankton using ocean-colour data. *Marine ecology progress series*, 272:59–68, 2004.

Alexander F Schober, Carolina Río Bártulos, Annsophie Bischoff, Bernard Lepetit, Ansgar Gruber, and Peter G Kroth. Organelle studies and proteome analyses of mitochondria and plastids fractions from the diatom thalassiosira pseudonana. *Plant and Cell Physiology*, 60(8):1811–1828, 2019.

Joseph Seckbach and Patrick Kociolek. *The diatom world*, volume 19. Springer Science & Business Media, 2011.

Maximilian Seeger. Digitale narrative in mikrokosmos - jewels of the sea. Master's thesis, Hochschule fr angewandte Wissenschaften Wrzburg, Schweinfurt, Germany, 7 2021. B.S. Thesis.

Ikuko Shihira-Ishikawa, Takanori Nakamura, Sho-ichi Higashi, and Masakatsu Watanabe. Distinct responses of chloroplasts to blue and green laser microbeam irradiations in the centric diatom pleurosira laevis. *Photochemistry and photobiology*, 83(5):1101–1109, 2007.

John P Smol and Eugene F Stoermer. *The diatoms: applications for the environmental and earth sciences*. Cambridge University Press, 2010.

V Stuart, S Sathyendranath, EJH Head, T Platt, B Irwin, and H Maass. Bio-optical characteristics of diatom and prymnesiophyte populations in the labrador sea. *Marine Ecology Progress Series*, 201:91–106, 2000.

Yanyan Su, Nina Lundholm, Søren MM Friis, and Marianne Ellegaard. Implications for photonic applications of diatom growth and frustule nanostructure changes in response to different light wavelengths. *Nano Research*, 8(7):2363–2372, 2015.

Jiyu Sun, Bharat Bhushan, and Jin Tong. Structural coloration in nature. *Rsc Advances*, 3(35):14862–14889, 2013.

Lucilla Taddei, Giulio Rocco Stella, Alessandra Rogato, Benjamin Bailleul, Antonio Emidio Fortunato, Rossella Annunziata, Remo Sanges, Michael Thaler, Bernard Lepetit, Johann Lavaud, et al. Multisignal control of expression of the LHCX protein family in the marine diatom *Phaeodactylum tricornutum*. *Journal of Experimental Botany*, 67(13):3939–3951, 2016.

Allen Taflove and Susan C Hagness. Computational electromagnetics: the finite-difference time-domain method. *Artech House*, 3, 2000.

Allen Taflove, Susan C. Hagness, and Melinda Piket-May. Computational electromagnetics: The finite-difference time-domain method. In Wai-Kai Chen, editor, *The Electrical Engineering Handbook*, pages 629–670. Elsevier, 2005.

P Vukusic, JR Sambles, CR Lawrence, and RJ Wootton. Quantified interference and diffraction in single morpho butterfly scales. *Proceedings of the Royal Society of London. Series B: Biological Sciences*, 266(1427):1403–1411, 1999.

Pete Vukusic and J Roy Sambles. Photonic structures in biology. *Nature*, 424 (6950):852–855, 2003.

Anya Waite, Anne Fisher, Peter A Thompson, and Paul J Harrison. Sinking rate versus cell volume relationships illuminate sinking rate control mechanisms in marine diatoms. *Marine Ecology Progress Series*, 157:97–108, 1997.

Wenda Wang, Songhao Zhao, Xiong Pi, Tingyun Kuang, Sen-Fang Sui, and Jian-Ren Shen. Structural features of the diatom photosystem ii–light-harvesting antenna complex. *FEBS journal*, 287(11):2191–2200, 2020.

Charles H Whitlock, David S Bartlett, and Ernest A Gurganus. Sea foam reflectance and influence on optimum wavelength for remote sensing of ocean aerosols. *Geophysical Research Letters*, 9(6):719–722, 1982.

Heather M Whitney, Mathias Kolle, Piers Andrew, Lars Chittka, Ullrich Steiner, and Beverley J Glover. Floral iridescence, produced by diffractive optics, acts as a cue for animal pollinators. *Science*, 323(5910):130–133, 2009.

Shigeru Yamanaka, Rei Yano, Hisanao Usami, Nobuaki Hayashida, Masakatsu Ohguchi, Hiroyuki Takeda, and Katsumi Yoshino. Optical properties of diatom silica frustule with special reference to blue light. *Journal of Applied Physics*, 103(7):074701, 2008.